Heating and Moistening of the MJO during DYNAMO in ECMWF Reforecasts

JI-EUN KIM

Rosenstiel School of Marine and Atmospheric Science, University of Miami, Miami, Florida, and Joint Institute for the Study of the Atmosphere and Ocean, University of Washington, Seattle, Washington

CHIDONG ZHANG

NOAA/Pacific Marine Environmental Laboratory, Seattle, Washington

GEORGE N. KILADIS

NOAA/Earth System Research Laboratory, Boulder, Colorado

PETER BECHTOLD

European Centre for Medium-Range Weather Forecasts, Reading, United Kingdom

(Manuscript received 2 June 2017, in final form 1 December 2017)

ABSTRACT

Reforecasts produced by the ECMWF Integrated Forecast System (IFS) were used to study heating and moistening processes associated with three MJO events over the equatorial Indian Ocean during the Dynamics of the Madden–Julian Oscillation (DYNAMO) field campaign. Variables produced by and derived from the IFS reforecast (IFS-RF) agree reasonably well with observations over the DYNAMO sounding arrays, and they vary smoothly from the western to eastern equatorial Indian Ocean. This lends confidence toward using IFS-RF as a surrogate of observations over the equatorial Indian Ocean outside the DYNAMO arrays. The apparent heat source Q_1 and apparent moisture sink Q_2 produced by IFS are primarily generated by parameterized cumulus convection, followed by microphysics and radiation. The vertical growth of positive Q_1 and Q_2 associated with the progression of MJO convection can be gradual, stepwise, or rapid depending on the event and its location over the broader equatorial Indian Ocean. The time for convective heating and drying to progress from shallow (800 hPa) to deep (400 hPa) can be $<$1 to 6 days. This growth time of heating and drying is usually short for convective processes alone but becomes longer when additional microphysical processes, such as evaporative moistening below convective and stratiform clouds, are in play. Three ratios are calculated to measure the possible role of radiative feedback in the MJO events: amplitudes of radiative versus convective heating rates, changes in radiative versus convective heating rates, and diabatic (with and without the radiative component) versus adiabatic heating rates. None of them unambiguously distinguishes the MJO from non-MJO convective events.

1. Introduction

During the Dynamics of the Madden–Julian Oscillation (DYNAMO)[1] field campaign (Yoneyama et al. 2013), two quadrilateral sounding arrays were formed with six sites (two ships and four islands) over the equatorial central Indian Ocean (Fig. 1). Intensive sounding observations (eight per day) were taken during the special observing period (SOP) of 1 October–15 December 2011 from the arrays, which were reduced to triangles for short periods of ship port calls and after the SOP (Johnson and Ciesielski 2013). The northern sounding array (NSA) extended from the equator to about 4° and 7°N and from 73° to 80°E. Three Madden–Julian oscillation (MJO) events (Madden and Julian 1971, 1972) passed through this array during

[1] DYNAMO is a joint project with the Cooperative Indian Ocean Experiment on Intraseasonal Variability in the Year 2011 (CINDY2011), ARM MJO Investigation Experiment (AMIE), and Littoral Air–Sea Process (LASP).

Corresponding author: Ji-Eun Kim, jkjkjk@uw.edu

DOI: 10.1175/JAS-D-17-0170.1

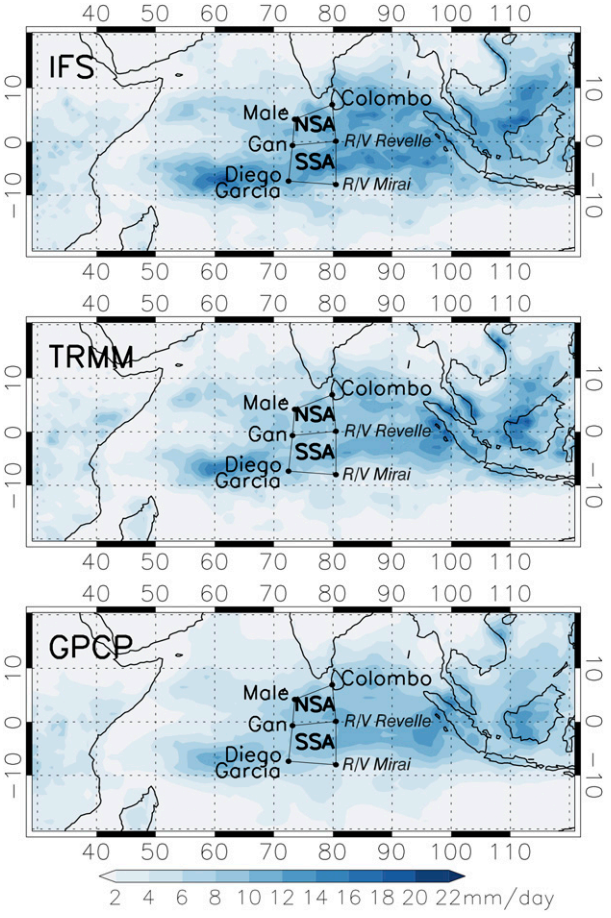

FIG. 1. DYNAMO NSA and SSA with mean precipitation from (top to bottom) IFS, TRMM, and GPCP for October–December 2011. The mean over the BSA (NSA + SSA) is 10.9, 8.5, and 9.0 mm day^{-1} in IFS, TRMM, and GPCP, respectively.

DYNAMO (Gottschalck et al. 2013). Many interesting processes have been revealed by analyses of the soundings (Johnson and Ciesielski 2013; Johnson et al. 2015; Sobel et al. 2014; Ciesielski et al. 2017). For example, gradual moistening from the lower to midtroposphere took place over approximately 2-week periods during MJO initiation. Patterns of moistening, divergence, and vertical motion in the sounding observations suggest a stepwise progression of convection, from shallow cumulus to congestus to deep convection. Gravity or Kelvin waves within and near MJO convective envelopes modulated the tropopause and contributed to upper-tropospheric moistening prior to MJO initiation. While both horizontal and vertical advection help moisten the lower atmosphere during the buildup to active phases of the MJO, they dry the atmosphere in the wake of the active phase. Observed fluctuations in radiative anomalies suggest that they play a significant role in the growth and maintenance of the MJO and that radiative–convective instability might be operative for the DYNAMO MJO events based on a ratio of radiative to convective heating.

The southern sounding array (SSA) was at similar longitudes as the NSA, extending from the equator to about 8°S. When observations from the NSA indicate a convectively suppressed period prior to MJO initiation, active convection associated with the intertropical convergence zone (ITCZ) was generally located over the SSA (Yoneyama et al. 2013; Kerns and Chen 2014). As MJO convection initiated and strengthened, it covered a broader area including both sounding arrays (BSA). Rainfall in the SSA during basinwide active periods of the MJO was stronger than during the local ITCZ periods but weaker than in the NSA. A stratiform rain fraction was greater in the NSA than SSA (Johnson et al. 2015).

Observations from the DYNAMO sounding arrays are but one example of the indispensable role of soundings collected from field campaigns in advancing our knowledge and understanding of the vertical structure of the atmosphere, especially gross features of interaction between convective systems and their large-scale environment. In addition to direct observations of the standard fields—winds, temperature, humidity, and pressure—equally important quantities derived from these directly measured fields are the apparent heat source Q_1 and moisture sink Q_2 in the temperature and humidity tendency equations (Yanai et al. 1973). They represent all processes contributing to temperature and humidity tendencies that cannot be directly observed by soundings. They also include errors in estimating areal mean quantities using measurements at the limited number of points that form a sounding array. For this latter reason, the size and shape of an array is an important factor to its accuracy in estimated Q_1 and Q_2 (Katsumata et al. 2011). Numerical errors in estimating Q_1 and Q_2 using a limited number of points can be demonstrated by comparing Q_1 and Q_2 calculated from the temperature and humidity tendency equations to those as combinations of all tendency terms from parameterization schemes of a numerical model. Their differences are evident, even though their large-scale distributions and variations associated with the MJO are similar (Ling and Zhang 2011). Given such errors, Q_1 and Q_2 estimated from soundings are still the only observationally based information available of all unresolved physical processes in combination for temperature and humidity tendencies.

There are two other limitations of Q_1 and Q_2 estimated from sounding observations. The first is that there is no separation of individual processes that contribute to Q_1 and Q_2. These processes include microphysics, turbulence, radiation, and gravity waves (Yanai et al. 1973). The second is that their coverage is limited in space and time. There are two ways to address these two limitations.

One is to use data assimilation products that include individual tendency terms from parameterization schemes with global and long-term coverage. Examples of such products are the Modern-Era Retrospective Analysis for Research and Applications (MERRA; Rienecker et al. 2011; Mapes and Bacmeister 2012) and Year of Tropical Convection (YOTC) European Centre for Medium-Range Weather Forecasts database, known as the YOTC analysis (Moncrieff et al. 2012; Waliser et al. 2012). Obviously, these products include errors from parameterization schemes. Cloud-permitting model (CPM) simulations constrained by sounding observations (Tao et al. 2004) are commonly used to mitigate errors from cumulus parameterization schemes but are still subject to sensitivities to parameterization of other physical processes, such as microphysics (e.g., Li et al. 2009).

Simulations by large-eddy simulation (LES) models and CPMs constrained by DYNAMO observations were made to reproduce detailed processes not observed by DYNAMO soundings (Skyllingstad and de Szoeke 2015; Takemi 2015; Wang et al. 2015; Janiga and Zhang 2016; Wang et al. 2016). It was found that low-level moistening preceding the passage of the MJO is dominated by the effects of shallow precipitating clouds. Eddy transport by congestus and deep convective clouds contribute to subsequent mid- and upper-level moistening, respectively, as well as low-level drying. Non-precipitating clouds mainly modulate the column-confined moisture tendency through their effects on radiation. Local surface evaporation contributes much less to the overall moisture budget of the troposphere. Longwave cooling affects vertical motion and drying in both suppressed and active phases. Large-scale horizontal advection is responsible for much of the drying during the transition from convectively active to suppressed phases, as directly observed from the soundings. Some of these results are sensitive to microphysics parameterization schemes.

Beyond the DYNAMO sounding arrays, sounding observations are available at certain locations, and they have been used to diagnose the atmospheric structure outside the sounding arrays (Kubota et al. 2015; Yokoi and Sobel 2015), but their coverage is also limited. CPMs covering a large domain (e.g., the tropical Indian Ocean) were used to produce variability of cloud and circulation associated with one or two MJO events during DYNAMO (Hagos et al. 2014a,b; Wang et al. 2016). Another version of a regional model configuration consists of nested domains with CPM resolution covering the sounding array (Chen et al. 2015). These models were constrained by using initial and boundary conditions from global reanalysis products. Because of their high resolutions, those results were compared to field observations from radars as well as soundings, with very encouraging results.

Global models were also used to produce the large-scale features of the MJO events during DYNAMO. These models are either of low resolution with cumulus parameterization (Hannah and Maloney 2014) or high resolution without cumulus parameterization (Miyakawa et al. 2014). A global model consisting of variable grids with regional refinement over the Indian Ocean has also been used, in which cumulus parameterization was used only outside the regional refinement domain (Pilon et al. 2016). These models are constrained by observations only through the initial conditions and prescribed sea surface temperature, unless they are coupled (Fu et al. 2015). Results from these global models are usually validated against gridded global reanalysis products and satellite observations, except for the case with regional refinement, from which results can be compared directly to radar as well as sounding observations.

Each numerical approach, from simulations by LES and CPMs to those by regional and global models, provides additional information unavailable from sounding observations alone (e.g., individual processes responsible for temperature and humidity tendencies along with large-scale structures), but each also suffers from its own sources of errors. Ultimately, our knowledge and understanding of the physical processes of the DYNAMO MJO events must be built upon accumulated information from observations, data assimilation products, and numerical model simulations.

Data assimilation products are powerful tools for diagnosing large-scale processes during DYNAMO, especially the advection of momentum, moisture, and temperature (Li et al. 2015; Nasuno et al.2015; Oh et al. 2015; Tseng et al. 2015). Temperature and moisture tendencies representing physical processes (cumulus convection, clouds and large-scale precipitation, turbulence, radiation, and gravity waves) are needed for diagnosing details in temperature and moisture evolution. For this study, a reforecast product for DYNAMO was produced by the most advanced version of the ECMWF Integrated Forecast System (IFS; cycle Cy43r1) that includes many improvements from the model that produces the ERA-Interim product. This reforecast product includes, in addition to the conventional variables, all the tendency terms for temperature and moisture due to both resolved processes (advection) and parameterized processes.

The objectives of this study are 1) to determine if we can use this IFS reforecast product as a surrogate for observations and, if we can, 2) to examine the degree to which the structural evolution of heating and moistening associated with the MJO observed during DYNAMO by the sounding data is also present in other areas over the

equatorial Indian Ocean outside the sounding arrays, and 3) to investigate the individual processes that contribute to the total heating and drying (Q_1 and Q_2). Objective 3 will emphasize radiative contributions to Q_1, because it is the only individual tendency term from the IFS reforecast product that can be validated against observations to a certain degree. We focus on the structural evolution of Q_1, Q_2, and their individual components.

We introduce the data used in section 2. In section 3, the IFS reforecast product is compared against DYNAMO and other observations to assess its reliability. Results from section 3 suggest the IFS reforecast can be used as a surrogate of observations, which leads to section 4, where it is used to demonstrate contributions to Q_1 and Q_2 by individual components over a broad equatorial region of the Indian Ocean. The possible role of radiation in the MJO is specifically examined in the same section. A summary and discussion are given in section 5.

2. Data

ECMWF IFS reforecasts (IFS-RF) were made for the DYNAMO period (1 October 2011–31 January 2012) using the model cycle of Cy43r1 (implemented in November 2016) with horizontal resolution of TCo639 (~16 km) and 137 vertical levels. DYNAMO sounding observations were submitted to global telecommunication satellites (GTS) and assimilated into the IFS model. Only microwave all-sky humidity sounders were used for precipitation assimilation. The model was initialized daily at 0000 UTC. Daily means of 3-hourly output during the first 24 h from the initialization were used in this study to minimize errors by forecast drift. Data of the standard fields, cloud information, and tendency terms were interpolated onto a $1° \times 1°$ horizontal-resolution grid at the surface and 23 pressure levels from 1000 to 10 hPa with vertical resolution of 50 hPa at 900–100 hPa and 25 hPa at 1000–900 hPa. The apparent heat source Q_1 and apparent moisture sink Q_2 were calculated from daily means of $1° \times 1°$ horizontal-resolution data.

DYNAMO $1° \times 1°$ gridded sounding data (version 3a) were derived from rawinsonde observations and other sources including satellites and dropsondes without input from global data assimilation products (Johnson and Ciesielski 2013; Ciesielski et al. 2014; Johnson et al. 2015). This dataset includes basic variables (temperature T, specific humidity q, zonal wind u, and meridional wind v) and derived variables (vertical pressure velocity ω, Q_1, and Q_2) at 25-hPa vertical resolution from 1000 to 50 hPa. For comparisons with IFS-RF, we use the gridded sounding data only at the vertical levels where IFS-RF is available. The derived variables are more reliable when soundings were launched simultaneously at all six sites of the two DYNAMO arrays (Fig. 1) than during the periods of port calls of the ships (R/V *Revelle* and *Mirai*) that formed two eastern corners of the sounding arrays or after their cruises ended (Ciesielski et al. 2014). This gridded DYNAMO sounding data will be referred to as the DYNAMO observations.

The accuracy of IFS-RF was evaluated against data from several sources as well as the DYNAMO observations. The Tropical Rainfall Measuring Mission (TRMM) 3B42, version 7 (Huffman et al. 2007), data were used for comparisons of precipitation. These daily data at 0.25° horizontal resolution were interpolated onto a $1° \times 1°$ horizontal grid. We also used GPCP One-Degree Daily (1DD), version 1.2 (Huffman et al. 2001), daily precipitation at 1° resolution. Radiative heating profiles at Gan Island, Maldives, from the Pacific Northwest National Laboratory (PNNL) Combined Retrieval (CombRet) and Clouds and the Earth's Radiant Energy System (CERES) data were also used. CombRet radiation profiles were estimated using observations of radars and soundings on Gan Island during DYNAMO (Feng et al. 2014). The CERES product was derived from satellite observations of short- and longwave fluxes at the top of the atmosphere. Additional in-atmosphere fluxes at 500, 200, and 70 hPa at 1° horizontal resolution in CERES were estimated using cloud properties from Moderate Resolution Imaging Spectroradiometer (MODIS; Wielicki et al. 1996), providing radiation information between these vertical levels.

3. Validation of IFS-RF over the DYNAMO arrays

In this section, we compare IFS-RF to observations introduced in section 2. The main purpose of such a comparison is to demonstrate the extent to which the IFS-RF can be used as a surrogate for observations in regions of the equatorial Indian Ocean where no sounding observations are available. Except for precipitation, comparisons are made over both DYNAMO sounding arrays (BSA) combined. The reason for this is that most studies of the MJO present large-scale analysis for the equatorial region without distinguishing between areas north and south of the equator.

a. Precipitation

Figure 1 compares the mean precipitation from IFS-RF, TRMM, and GPCP for October–December 2011. The IFS-RF produces similar geographical patterns of precipitation as TRMM and GPCP over the Indian Ocean. All show a swallowtail pattern with a minimum at the equator, typical for the west side of MJO precipitation (Zhang and Ling 2012). Mean precipitation is slightly stronger in IFS-RF than in TRMM and GPCP,

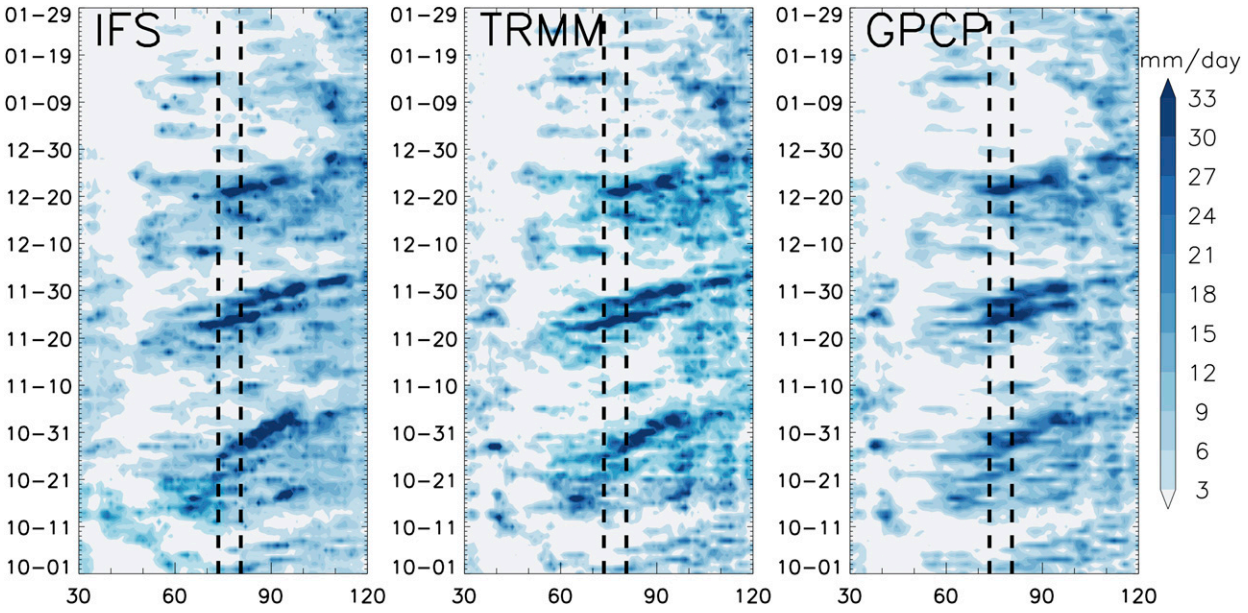

FIG. 2. Time–longitude diagrams of daily precipitation (mm day^{-1}) averaged over 5°S–5°N for October 2011 to January 2012 from IFS, TRMM, and GPCP. Two dashed lines represent zonal boundaries of the DYNAMO sounding arrays.

but its overall mean values in the three are quite comparable throughout the domain. Johnson et al. (2015) showed that the mean precipitation derived from DYNAMO sounding budgets slightly exceeds the satellite estimates, indicating there might be uncertainties in the TRMM and GPCP data. Xu and Rutledge (2015) showed that the TRMM product underestimates rainfall during suppressed periods and tends to overestimate during the convectively active phases. The time–longitude diagrams in Fig. 2 and time series of precipitation from each dataset in Fig. 3 indeed demonstrate that IFS-RF precipitation generally exceeds TRMM estimates during convectively suppressed phases, resulting in slightly higher mean values in IFS-RF.

Despite uncertainties in rainfall estimates, the IFS nonetheless captures the timing and location of three observed large-scale events of slow propagation in precipitation over the Indian Ocean and Maritime Continent as well as many of the other details of the higher-frequency precipitation variability during DYNAMO (Fig. 2). The three eastward-propagating large-scale signals in precipitation have been identified as three MJO events (Gottschalck et al. 2013). They will be referred to as the October, November, and December events in this study, respectively. While the three MJO events commonly include convectively coupled Kelvin waves, their detailed characteristics are different in terms of relative activity of different types of disturbances that are embedded within their convective envelope (Kikuchi et al. 2018). The November event has the strongest Kelvin wave signals: one proceeds the MJO over the western Indian Ocean, and the decay of the second Kelvin wave within the MJO coincides with the decay of MJO convection (Fig. 2). The December MJO is by far the weakest, and its OLR and precipitation signal associated with the MJO begins near the central Indian Ocean while the other two events are initiated over the western Indian Ocean (Gottschalck et al. 2013; Kikuchi et al. 2018). All these observed features were reproduced in IFS-RF in Fig. 2 to a certain degree. Time series of precipitation averaged over the sounding arrays confirm that the amplitudes of the precipitation from the IFS, TRMM, and GPCP agree generally very well in the central Indian Ocean, with detailed discrepancies nonetheless (Fig. 3). MJO-related precipitation with higher peaks are seen in the NSA, while higher-frequency disturbances superimposed on the three MJOs are more active in the SSA (Johnson et al. 2015). Correlation coefficients between time series of precipitation datasets from daily IFS and TRMM are 0.7–0.9 over these regions, confirming the precipitation evolution is well captured by the IFS.

b. *Basic dynamical variables*

We compare basic variables such as temperature (T), zonal wind (u), meridional wind (v), vertical velocity (ω), specific humidity (q), and relative humidity (RH) from the IFS-RF and the sounding observations as BSA averages for October–November 2011. Since the sounding observations are most reliable for the period from 1 to 24 October and 10 to 28 November when the two ships were both at their nominal locations, we exclude data for

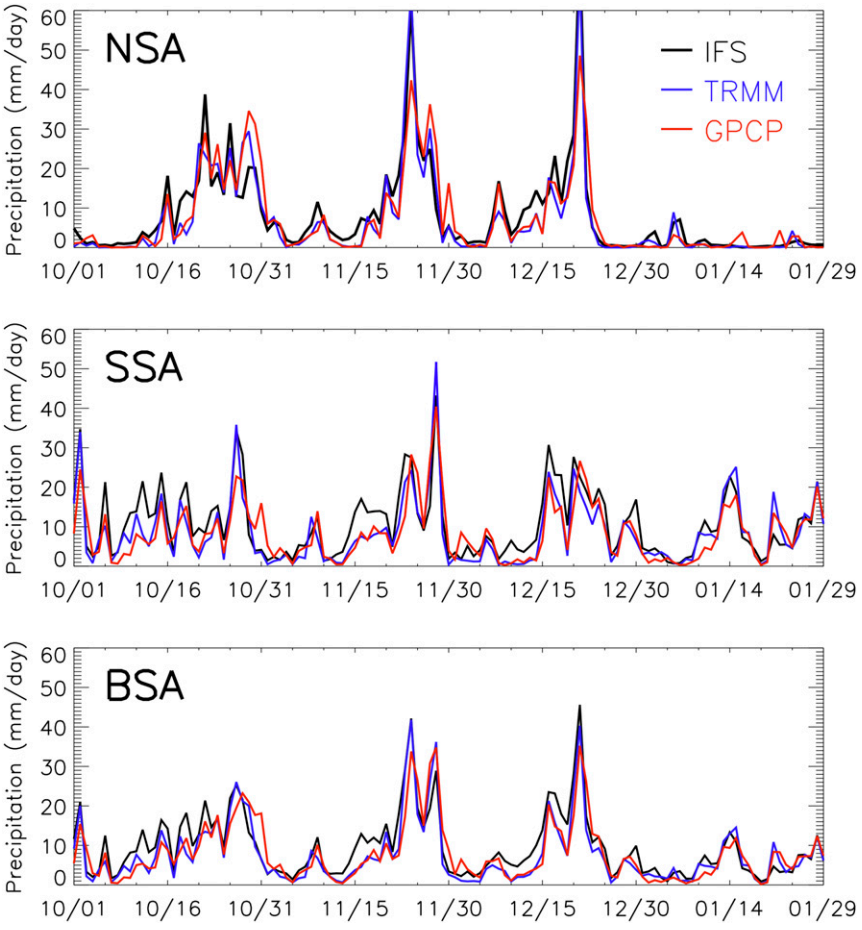

FIG. 3. Daily mean time series of precipitation from IFS (black), TRMM (blue), and GPCP (red) averaged over the DYNAMO sounding arrays: (a) NSA, (b) SSA, and (c) BSA.

December in this comparison. Although the sounding array was incomplete for short time segments, data for the whole months of October and November are compared to capture the two complete cycles of MJOs.

Figure 4 shows that the basic variables are generally in good agreement as measured by vertical profiles of mean biases of IFS-RF (mean differences from the observations) and variability (standard deviations). The IFS-RF tends to produce dry and cool biases in the lower troposphere, especially near the surface, which is consistent with results from Nagarajan and Aiyyer (2004), yielding a root-mean-square error (RMSE) greater than one standard deviation. The dry bias in q near the surface mainly comes from model spinup. This bias is reduced from 0–12 to 12–24 and 24–36 h (not shown). Standard deviations of q from IFS-RF and the observations match well at all levels, indicating that the IFS captures moisture variability despite the negative mean bias at lower levels. On the other hand, variability in ω is slightly stronger in IFS-RF than in the observations, resulting in large RMSE, in spite of the small mean bias throughout the troposphere. This is presumably related to slightly stronger convection in IFS-RF during active MJOs, which will be discussed in section 3d. Large RMSE in ω was also detected in ERA-Interim during DYNAMO (Pilon et al. 2016). The IFS overestimates mean relative humidity by 5%–10% in the upper troposphere compared to the observations because of a slight cold bias. This is associated with an overestimation of upper-level cloudiness in IFS-RF, but standard deviations of relative humidity from the IFS and soundings agree reasonably well with each other.

The agreement between the observations and IFS-RF cannot be attributed entirely to the assimilation of the observations. Because of the variety of observational sources for IFS data assimilation, forecast skill of the IFS for the DYNAMO MJO events is not entirely dependent on the DYNAMO sounding observations (Ling et al. 2014).

c. *Radiative heating*

For comparisons of radiative heating profiles, we took time series from the IFS-RF and CERES at grid points

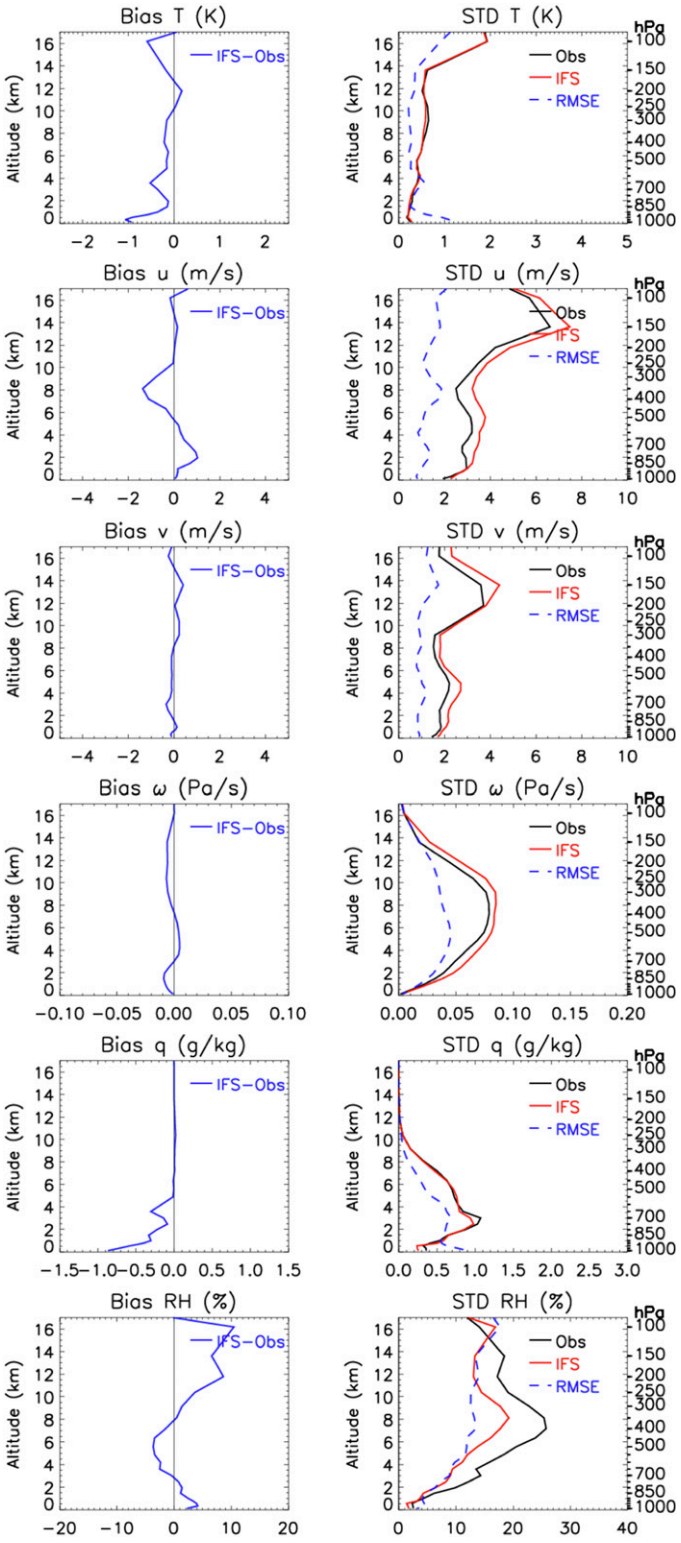

FIG. 4. (left) IFS mean biases of (top to bottom) temperature (T), zonal wind (u), meridional wind (v), vertical pressure velocity (ω), specific humidity (q), and RH relative to the sounding observations over the BSA for October–November 2011. The comparison is for array averages from DYNAMO gridded sounding data and IFS-RF 1° interpolated fields. (right) Vertical profiles of standard deviations for the same variables as in the left panels from soundings (black) and IFS (red) and RMSE of daily fields between observations and IFS (blue dashed).

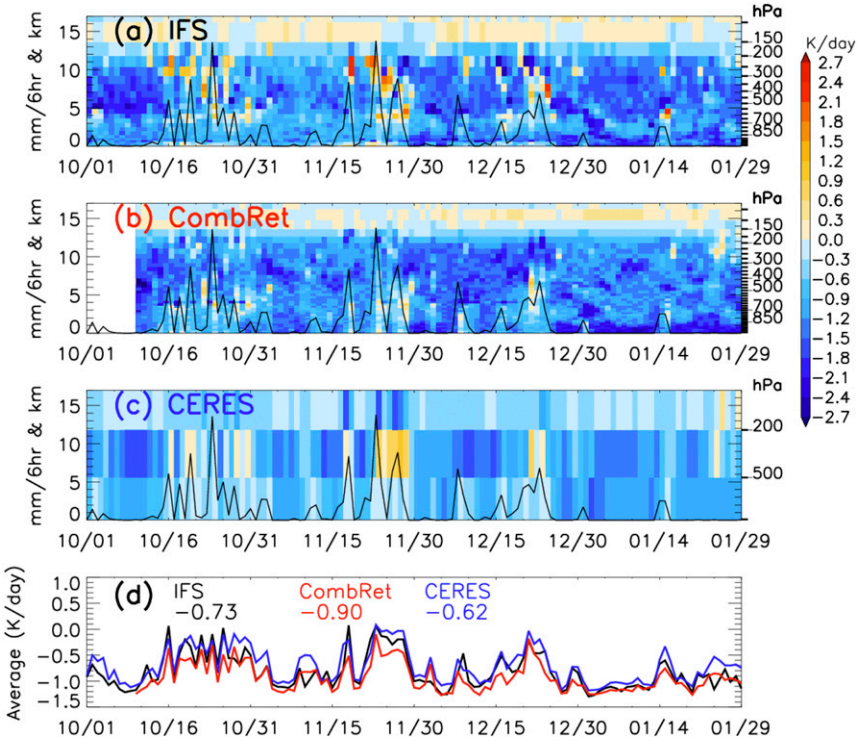

FIG. 5. Evolution of vertical structure of daily mean radiation over Gan Island in (a) IFS, (b) CombRet, and (c) CERES. The black curves in (a)–(c) are the daily mean time series of TRMM precipitation at Gan (mm $6\,h^{-1}$; left ordinate). The vertical resolutions of the figures correspond to that of each dataset. (d) Daily mean time series of column radiation averaged from 1000 to 70 hPa. Numbers correspond to the mean column-averaged radiation for October–December 2011.

closest to Gan Island where the CombRet estimates are based. Although the vertical resolutions of the three products are different, with CERES available only at few levels, their similarities and differences are evident (Figs. 5a–c). There is strong and persistent midlevel cooling punctuated by weak heating near the peaks of MJO rainfall (black curves). This MJO-related midlevel heating is the strongest in IFS-RF and weakest in CombRet. In IFS-RF, radiative heating in the upper layer leads strong precipitation and propagates downward. Similar downward-propagating signals in relative humidity and cloud fractions in the upper troposphere prior to deep MJO convection are also found (not shown). Virts and Wallace (2014) and Del Genio and Chen (2015) have shown signals of a gradual, downward increase in cirrus clouds from lidar data associated with the MJO. These signals imply the presence of waves (Virts and Wallace 2014; Kim et al. 2016) that yield enhanced cirrus clouds prior to the MJO passage. This downward upper-tropospheric radiative heating signal is not evident in CombRet, likely because of its limitations in detecting high cirrus clouds, which leads to its underestimation or complete omission of any positive net cloud radiative forcing in the upper troposphere (Yang et al. 2010).

The mass-weighted column-averaged radiative heating from 1000 to 70 hPa from all three products show a similar amount of net column cooling through the entire period of October–December 2011 (Fig. 5d). Their time series fluctuate in concert with TRMM precipitation (black line in Figs. 5a–c) for the three MJO events with, in general, less cooling in proportion to the amount of precipitation. Column radiative heating from IFS-RF is on average between the estimates from CombRet and CERES. Ciesielski et al. (2017) pointed out that CombRet suffers from a negative bias in this quantity because of its limitations in the detection of high cirrus clouds from ground-based radar. CERES might overestimate radiative heating (underestimate cooling) because of its radiative transfer model dependence on the MERRA reanalysis, which has biases in upper-level humidity. The actual radiative heating is likely bracketed by the estimates of CombRet and CERES because of these uncertainties. If so, the IFS-RF produces reasonable column-averaged radiative heating.

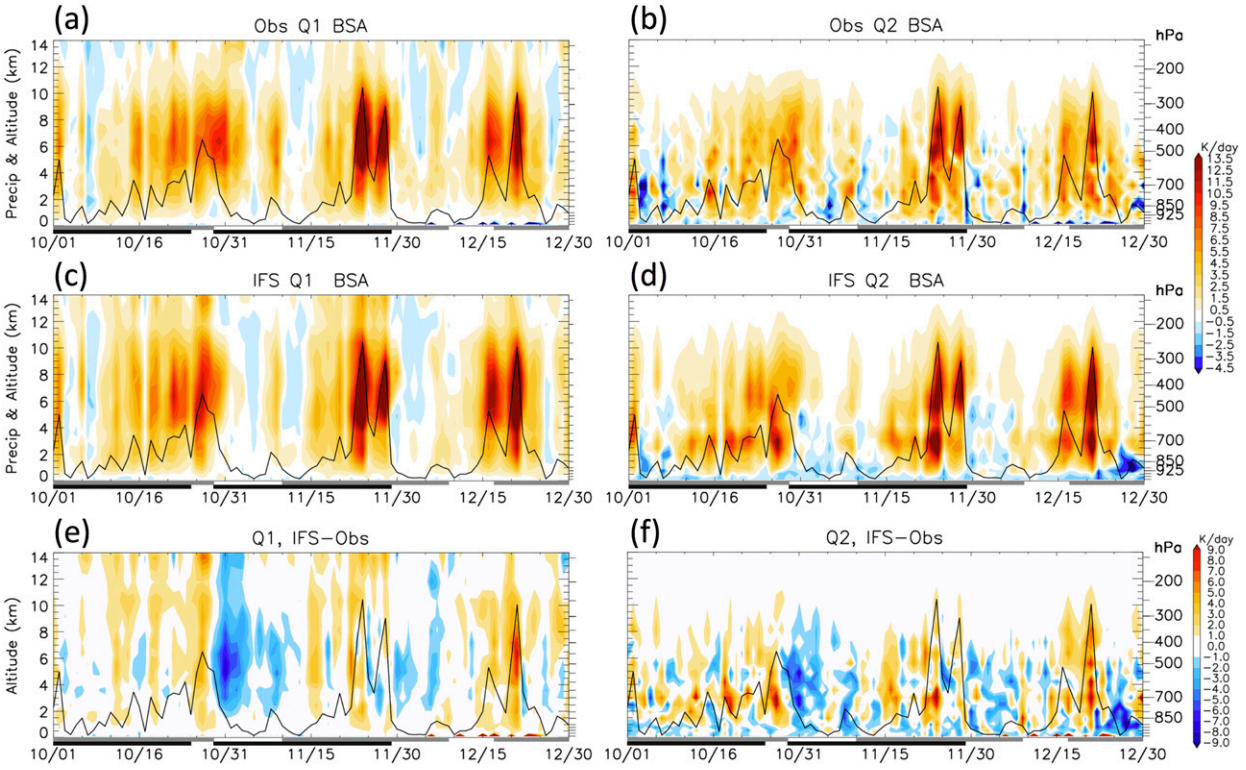

FIG. 6. Daily mean time series of (a) Q_1 and (b) Q_2 estimated from soundings and (c) Q_1 and (d) Q_2 from IFS, all averaged over the BSA. Differences between soundings and IFS are shown for (e) Q_1 and for (f) Q_2. TRMM precipitation (mm 6 h^{-1}; left ordinate) is overlaid at the bottom of each panel. Gray thick lines on the abscissa mark the time periods when R/V *Revelle* was on site, and black thick lines are for R/V *Mirai*.

d. Q_1 and Q_2

Following Yanai et al. (1973), the apparent heat source Q_1 and apparent moisture sink Q_2 are estimated as in the first lines of Eqs. (1) and (2):

$$Q_1 = \frac{\partial \overline{s}}{\partial t} + \overline{\mathbf{V}} \cdot \nabla \overline{s} + \overline{\omega} \frac{\partial \overline{s}}{\partial p} = \frac{\overline{Ds}}{Dt} - \frac{\partial \overline{\omega' s'}}{\partial p}, \quad (1)$$

$$Q_2 = -L_v \left(\frac{\partial \overline{q}}{\partial t} + \overline{\mathbf{V}} \cdot \nabla \overline{q} + \overline{\omega} \frac{\partial \overline{q}}{\partial p} \right) = -L_v \left(\frac{\overline{Dq}}{Dt} - \frac{\partial \overline{\omega' q'}}{\partial p} \right), \quad (2)$$

where s stands for dry static energy, $\mathbf{V}$ for horizontal velocity, ω for vertical pressure velocity, p for pressure, q for specific humidity, and L_v for the latent heat of vaporization. A bar represents an average over a given area, while a prime denotes unresolved perturbations within the area. In the second line of Eq. (1), term $\overline{Ds}/Dt$ represents the Lagrangian derivative of dry static energy, which is equivalent to the total heating tendency by all parameterized physical processes in IFS-RF. Similarly, $\overline{Dq}/Dt$ in Eq. (2) is the total moistening tendency by all physical processes. The horizontal components of the eddy flux terms are omitted in Eqs. (1) and (2) because of their negligible contributions relative to the vertical eddy fluxes (Yanai et al. 1973).

The evolution of vertical profiles of Q_1 and Q_2 derived from the sounding observations and IFS-RF using Eqs. (1) and (2) are generally in agreement for the three MJO events in terms of their sign, magnitude, vertical structure, and timing (Figs. 6a–d). There appear to be finer features in the observations than in the IFS. For all three MJO events, there are small positive biases in IFS-RF near the peaks of MJO deep convection and negative biases immediately after the rainfall peaks compared to observations (Figs. 6e and 6f). These suggest that MJO convection in the IFS-RF is slightly overestimated and decays slightly faster than in observations.

The largest discrepancy between the observations and IFS-RF in Q_1 is seen as an exaggerated midtropospheric cooling just after the October MJO (Fig. 6e). It is possible that this discrepancy is due to ship port calls making sounding-based observations less reliable. The melting level shows up clearly as a discontinuity in both Q_1 and Q_2 at around 550 hPa, and the main discrepancies in Q_2 exist around and especially below this level.

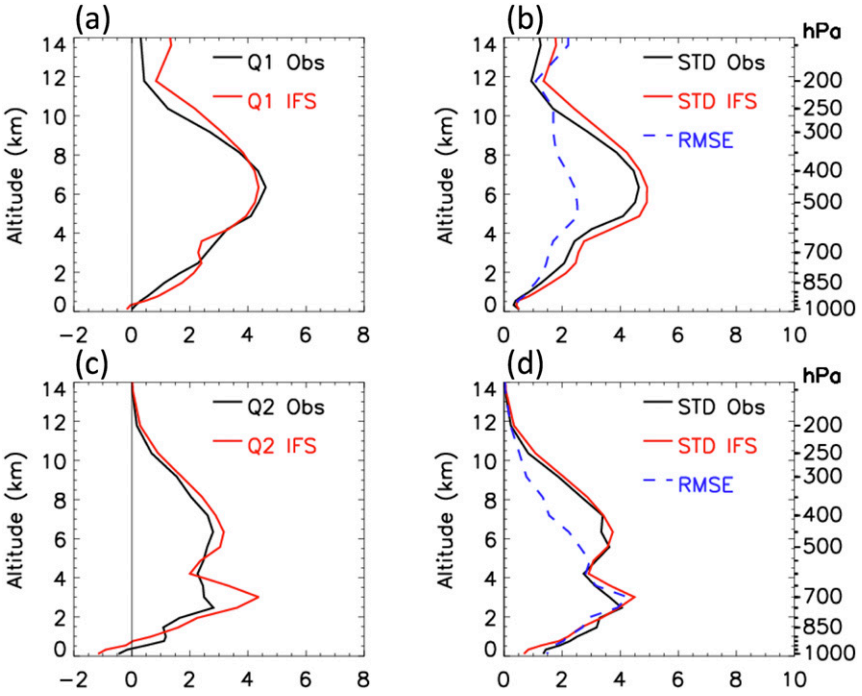

FIG. 7. Vertical structure of (a),(b) Q_1 and (c),(d) Q_2 over the BSA from the observations (black) and IFS (red) for (a),(c) their means and (b),(d) standard deviations of daily mean time series during October–November 2011. RMSEs (blue dashed) of IFS-RF are also included.

The largest errors in IFS-RF Q_2 are in a layer of 450–750 hPa, with stronger drying (positive tendencies) than in the observations (Figs. 6e and 6f). Overall, the observed evolution and amplitude of the major features of the three MJO events throughout the column are reasonably well captured by IFS-RF.

Figure 7 compares vertical structures of the time mean and daily standard deviations of Q_1 and Q_2 for the October–November 2011 period. The whole two months were included to capture the full cycles of the two MJO events despite brief periods of incomplete quadrilateral arrays due to ship port calls. The Q_1 profiles observed and produced by IFS-RF are close to each other, with slight overestimates in IFS-RF in the lower troposphere and above the 500-hPa level. There are discontinuities near the melting level and a double-peak structure in Q_2 seen in the IFS-RF, with maxima at 500 and near 700 hPa (Fig. 7c). Observed Q_2 profiles averaged over the BSA are smoother near the melting level, with the double-peak structure more evident in the standard deviation (Fig. 7d). The double-peak structure can be seen in time mean Q_2 profiles of the northern as well as southern sounding arrays (Johnson et al. 2015), which are smoothed out in the BSA average. The double-peak structure in Q_2 has been identified in previous field observations and ECMWF analysis for YOTC (Yanai et al. 1973; Johnson 1984; Esbensen et al. 1988; Katsumata et al. 2011; Klingaman et al. 2015). This suggests that the melting level discontinuity is common. Even assuming that the DYNAMO sounding observations of thermodynamic fields themselves are reliable, Q_2 is a derived quantity over an area roughly about the size of the sounding array without considering inputs from other sources. Although the estimated Q_2 from the DYNAMO observations used dropsonde and satellite input in addition to the radiosonde measurements, these datasets still have a limitation on resolving finescale features in moisture budgets. Hannah et al. (2016) showed that the DYNAMO sounding data produced errors in moisture budgets because of inaccurate representation of horizontal advection by synoptic-scale disturbances. This means that, while the sounding-derived Q_2 should well capture moistening–drying processes associated with advective moisture supply at scales larger than distances between soundings, or a few hundred kilometers with input from dropsonde and satellite data, it cannot resolve smaller-scale fluxes that may have measurable contributions to moisture processes near the melting level. This discrepancy might also be partly due to exaggeration of physical processes near the melting level in the IFS. With given data uncertainties and lack of our knowledge about processes of tropical convection and clouds near the melting level, we cannot determine the precise causes of the melting-level discrepancy in Q_2 between the DYNAMO observations and IFS-RF.

Despite the caveats that arise because of unresolved cloud processes near the melting level, the comparisons between IFS-RF and observations from DYNAMO and other sources indicate that the 0–24-h averages of IFS-RF are sufficiently close to the observations to be used as their surrogate. We will also take advantage of the fields that are not available from observations (e.g., individual tendency terms contributing to Q_1 and Q_2) and outside the DYNAMO sounding arrays. An implicit assumption is made here: if Q_1 and Q_2 from the IFS are reasonable in comparison to the observations, then their individual components are also within reasonable bounds. We have partially confirmed this for the radiation component of Q_1 in section 3c. The remaining two main diabatic components are produced by parameterization schemes for cumulus convection and microphysics. The realism of these two schemes is impossible to know without more detailed observations. We therefore put our faith in these components from the IFS, present their results in the next section, and trust that they will be further validated in the future.

4. Structural evolution of heating and moistening

In this section, we examine the structural evolution of heating and moistening processes as described by their various tendency terms produced by the IFS over the equatorial Indian Ocean (5°S–5°N, 50°–100°E). The first purpose of this exercise is to examine the degree to which observations for the DYNAMO sounding arrays can be extended to other longitudes of the equatorial Indian Ocean and thereby to assess the representativeness of the DYNAMO observations over its limited domain. The second purpose is to investigate the individual processes that contribute to the total heating and drying (Q_1 and Q_2) to the extent that we can trust them from IFS-RF.

a. DYNAMO sounding arrays (BSA)

IFS-RF data include contributions to the total temperature tendency from the parameterization schemes of convection, microphysics, radiation, turbulent diffusion, and gravity wave drag. These in combination yield the total Lagrangian change in heat (dry static energy), $\overline{Ds}/Dt$, in Eq. (1). The total Lagrangian change in moisture, $\overline{Dq}/Dt$, is a combination of moisture tendencies produced by parameterization schemes of convection, microphysics, and turbulent diffusion. Thus, these terms can be expressed as

$$\frac{\overline{Ds}}{Dt} = Q_T = Q_{\text{con}} + Q_{\text{mic}} + Q_{\text{diff}} + Q_{\text{drag}} + Q_{\text{rad}}, \quad (3)$$

$$-L_v\frac{\overline{Dq}}{Dt} = M_T = M_{\text{con}} + M_{\text{mic}} + M_{\text{diff}}, \quad (4)$$

where Q represents heating from the convective scheme (with subscript con), microphysics (mic), turbulent diffusion (diff), gravity wave drag (drag), radiation (rad), and their combination (T); M represents moisture sinks from the same schemes.

The convection scheme in the IFS represents all moist convective processes from shallow, midlevel (elevated moist layers), congestus, and deep convection. The mass flux of deep convection is determined by a CAPE closure, and shallow convection is based on the moist static energy budget. The scheme was originally described in Tiedtke (1989) and has been modified over time to include, for example, changes in the entrainment formulation (Bechtold et al. 2008) and CAPE closure (Bechtold et al. 2014). The microphysics scheme represents the sources and sinks of water vapor due to processes outside convective plumes, including detrainment from cumulus convection and condensation from nonconvective processes such as large-scale lifting of moist air and radiative cooling. The scheme is based on Tiedtke (1993) with an enhanced representation of mixed-phase clouds (Forbes and Tompkins 2011; Forbes et al. 2011) and ice supersaturation (Tompkins et al. 2007). The radiative transfer model in the IFS interactively calculates shortwave and longwave radiation by predicted clouds, temperature, and water vapor using a prescribed monthly climatology of aerosols and main trace gases.

We rewrite Eqs. (1) and (2) as follows:

$$Q_1 = Q_T + F_s, \quad (5)$$

$$Q_2 = M_T - F_q, \quad (6)$$

where

$$F_s = -\frac{\partial\overline{\omega' s'}}{\partial p}, \quad (7)$$

$$F_q = -L_v\frac{\partial\overline{\omega' q'}}{\partial p}. \quad (8)$$

The quantities F_s and F_q are small-scale vertical eddy fluxes of dry static energy and moisture, respectively (Figs. 8c,d). They were estimated as residuals using Q_T and M_T (Figs. 8a,b) and Q_1 and Q_2 (Figs. 6c,d) following Eqs. (5) and (6). Since we used 1° × 1° IFS-RF data to calculate Q_1 and Q_2, and subgrid-scale fluxes are represented in Q_T and M_T with parameterization schemes in the IFS, F_s and F_q represent eddy fluxes at scales larger than the IFS model grid (~16 km) and smaller than 1°. These eddy fluxes are much smaller than Q_1 and Q_2 so as a consequence, Q_T and M_T are very similar to Q_1 and Q_2 except for strong evaporative moisture flux near the surface (cf. Figs. 8a,b to Figs. 6c,d).

The main components contributing to Q_1 and Q_2 in the sounding arrays are those from convection, microphysics, and radiation (Fig. 9). Contributions from gravity wave drag and vertical diffusion are in general negligibly small above 950 hPa, but vertical diffusion is essential in the subcloud layer between 1000 and 950 hPa (Fig. 10). Near the surface, the convection scheme produces strong cooling and drying while turbulent diffusion produces strong heating and moistening. Although these values may seem large, there is good agreement of surface fluxes between the DYNAMO observations and IFS-RF (not shown), indicating that the combination of convective and turbulent fluxes has reasonable values. Nonetheless, we will hereafter focus on Q_1 and Q_2 and their contributing processes above the 950-hPa level.

In Fig. 9, the bulk of the heating and drying above 950 hPa during enhanced rainfall periods comes from contributions by the cumulus scheme. In comparison, the overall contribution from the microphysics scheme is much smaller but nonnegligible above the melting level (550 hPa). The mean moisture sink by the microphysics scheme becomes larger than that from the cumulus scheme in the upper troposphere above the 300-hPa level (purple and red lines in Fig. 10a). Heating and drying produced by the microphysics scheme are especially strong in the upper troposphere during and immediately after peak rainfall (Figs. 9b,e). This is an indication that heavy precipitation is generated by stratiform clouds with a top-heavy diabatic heating followed by deep convection (Powell and Houze 2013). Below the 500-hPa level, strong cooling associated with moistening occurs during active MJO periods, possibly because of evaporation of the rain drops.

Radiation cools the troposphere most of the time except for the upper troposphere during the active MJO phases, as also seen over Gan Island in the CombRet radar and CERES satellite estimates of Fig. 5. Its amplitude is much smaller than those of cumulus and microphysics schemes throughout the atmosphere except in the upper troposphere where the amplitude of radiative heating is comparable to those schemes.

b. *Equatorial Indian Ocean*

In this section, we examine the extent to which the structural evolution of heating and moistening in the DYNAMO arrays also exists over the rest of the equatorial Indian Ocean. To do this, we first selected several boxes of similar size as the DYNAMO arrays (10° longitude between 5°S and 5°N) located from the western to eastern Indian Ocean (Fig. 11). The box at 70°–80°E in Fig. 11 covers the DYNAMO sounding arrays (Fig. 1).

Main peaks in Q_1 and Q_2 occur in slightly later dates from the west to east (top to bottom rows in Fig. 11), indicating slow eastward propagation of the MJO. There is no discontinuity in the behavior of Q_1 and Q_2 seen in the IFS output between the DYNAMO arrays (70°–80°E) and the neighboring longitudes. This suggests that the agreement between Q_1 and Q_2 from the IFS-RF and the soundings over the DYNAMO array do not come only from the inclusion of the DYNAMO observations in IFS data assimilation. This lends confidence that the reliability of IFS-RF is comparable both inside and outside the DYNAMO arrays.

There is an interesting contrast in the behaviors of Q_1 and Q_2 from the west to east along the equator over the Indian Ocean. To the west, mean precipitation is weak or absent (Fig. 1a). Signals of the MJO in Q_1 and Q_2 are related to processes of convective initiation of the MJO in a relatively dry background. Over the eastern Indian Ocean near the Maritime Continent, convection is much more prevalent. Convective signals of the MJO there suggest a suppression of convective heating and drying in the wake of the MJO as well as enhancement during their peaks in the background of nearly persistent convection. There, no additional mechanism is needed to generate convection, which is typically present as seen in Figs. 1 and 2. The moistening effect of the transition from shallow to congestus clouds that is commonly hypothesized to be an important preconditioning for the development of deep convection of the MJO (Johnson et al. 1999; Benedict and Randall 2007) is probably not necessary to enhance existing active convection over the eastern Indian Ocean. Over the western part of the Indian Ocean, cloud evolution is thought to be essential to the buildup of widespread deep convection that creates the large-scale circulation pattern of the MJO, while over the eastern part, it is possible that clouds are more modulated by the MJO passage rather than playing a role of driving its propagation through cloud-induced moistening. This possibility is supported by our diagnostics of IFS-RF (not shown): mean relative humidity gradually increases from the western Indian Ocean to the Maritime Continent; over the western Indian Ocean, relative humidity exceeds 70% only during active MJO phases; over the Maritime Continent, however, relative humidity is above 70% most of the time, which can support widespread deep convection (Bretherton et al. 2004) regardless of the presence or absence of the MJO.

Shallow drying in the lower troposphere preceding deep-tropospheric drying by Q_2, observed over the DYNAMO arrays (Fig. 6b), can also be found outside the DYNAMO arrays, as shown in the right column in Fig. 11 for Q_2 and the left column in Fig. 12 for its anomalies. Anomalies are calculated as deviations

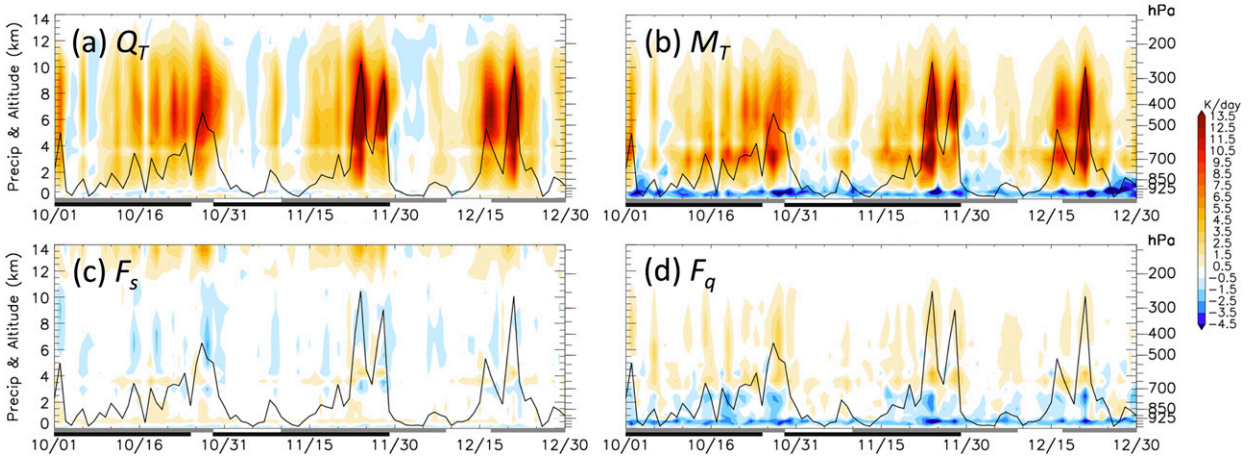

FIG. 8. Daily mean time series of (a) $Q_T = \overline{Dq}/Dt$, the total heating tendency, (b) $M_T = -L_v\overline{Dq}/Dt$, the total drying tendency by all parameterized physical processes in IFS, (c) F_s, the eddy flux of dry static energy, as a difference between Q_1 and Q_T, and (d) F_q, the eddy flux of moisture, as a difference between M_T and Q_2. Values are averaged over the BSA. Black curves are TRMM precipitation (mm $6\,h^{-1}$; left ordinate).

from a linear trend (as part of the seasonal cycle) at each vertical level during October–December 2011. Anomalies from the mean values also yield very similar results to Fig. 12. The transition from shallow to deep drying is gradual in smoothed or composite fields (Adames and Wallace 2015), but in observations of individual DYNAMO events, the transition can be stepwise (Johnson et al. 2015) and very fast (Powell and Houze 2013). There is a wide range (2–20 days) of shallow-to-deep transition time for MJO events (Xu and Rutledge 2016). The daily IFS Q_2 over the Indian Ocean in Fig. 12 suggests that the convective transition time for the same MJO event can also vary during its life cycle.

The direct output of convective drying, M_{con}, from the IFS allows us to examine the convective transition directly rather than just inferring it from Q_2. In the IFS, Q_2 is mainly composed of contributions from its cumulus parameterization scheme, M_{con}, and from its microphysics scheme, M_{mic}. Moistening/drying by microphysical processes are represented in both the cumulus and microphysics schemes. The deepening in Q_2 drying seen in its total (right column in Fig. 11) or anomalies (left column in Fig. 12) has been interpreted as progression of cloud populations from shallow to congestus and deep convection followed by stratiform precipitation (Johnson et al. 1999; Benedict and Randall 2007; Johnson et al. 2015). If so, and if Q_2 produced by the IFS represents the correct physical processes, this shallow-to-deep progression should be present in M_{con}. This is indeed the case but to a limited extent. The vertical structure of the drying anomalies contributed by M_{con} (middle panels in Fig. 12) is less tilted than Q_2 anomalies, indicating, as observed by DYNAMO radars (Powell and Houze 2013), that the transition from shallow to congestus and deep convection is faster than what can be inferred based on the Q_2 anomalies.

It is interesting to note that drying by M_{mic} appears to occur in two steps: weak at the low levels beneath deep-tropospheric moistening then strong and deep through most of the troposphere above moistening below. Upper-tropospheric peaks in M_{mic} slightly lag those in M_{con}. This vertical structural evolution of M_{mic}, in combination with that of M_{con}, comprises the gradual deepening in drying by Q_2. To the extent that the IFS-RF produces these processes correctly, gradual deepening in Q_2 drying is not solely due to the growth in depth of convective clouds but also due to changes in the large-scale conditions that might be an instigating factor rather than passive reaction to the cloud growth. Zermeño-Díaz et al. (2015) suggested that the observed gradual deepening in lower-tropospheric moisture leading to a peak of MJO convection over the western Pacific is more a consequence of the large-scale zonal moisture advection than cloud moistening. The importance of large-scale horizontal advection to the MJO has also been suggested by other studies (e.g., Sobel et al. 2014; Adames and Wallace 2015).

The gradual deepening of positive Q_2 anomalies during the convective buildup period has been described in terms of a westward upward-tilting structure in the horizontal–vertical cross section (Adames and Wallace 2015). The vertically tilted structure of Q_2 comes from a vertical dipole of positive anomalies on the top of negative anomalies in M_{mic} during the deep convective to stratiform period. The gradual increase in height of Q_2 anomalies is not exclusively due to the gradual growth of

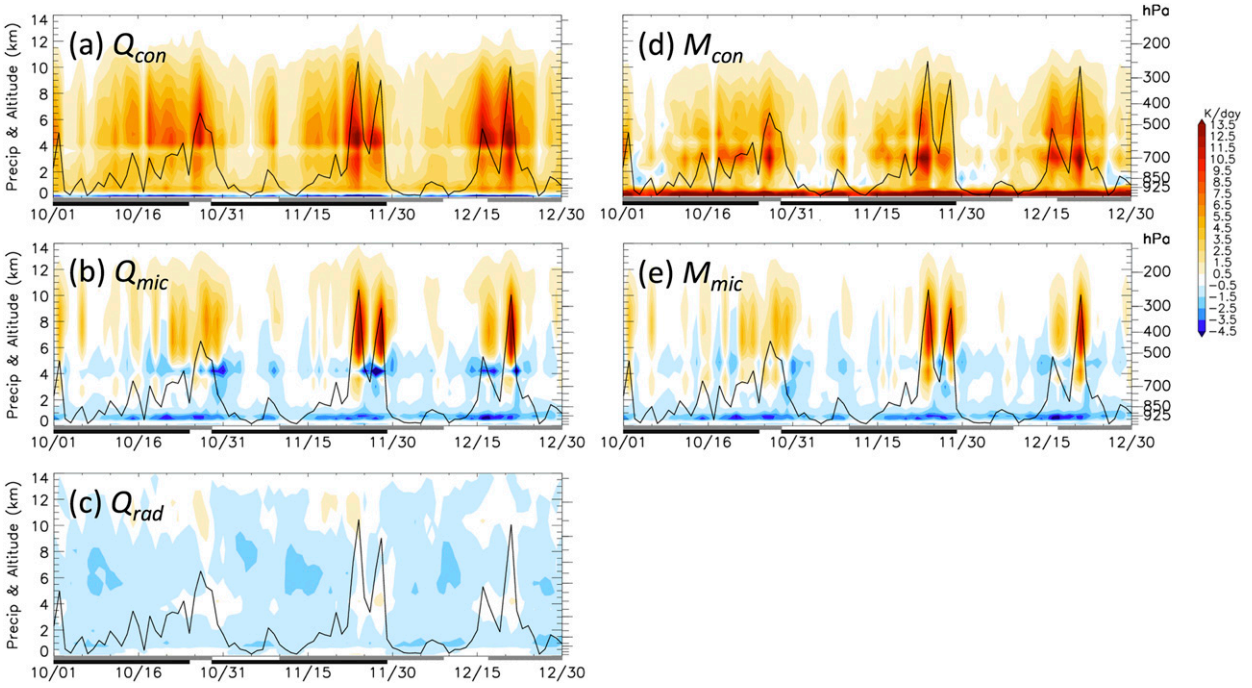

FIG. 9. Daily mean time series of IFS heating tendency by parameterization schemes of (a) convection, (b) microphysics, and (c) radiation, and drying tendency by parameterization schemes of (d) convection and (e) microphysics over the BSA. Black curves are for TRMM precipitation (mm $6\,h^{-1}$; left ordinate).

convective depth. It is also due to relatively less evaporative moistening (more positive contribution to Q_2 anomalies) in the lower troposphere during convectively inactive periods than active phases. In the upper troposphere, strong drying by condensation and deposition within stratiform clouds slightly lags a deep convection peak and is added to deep convective drying, enhancing the vertically tilted structure in Q_2. The importance of the tilted structure for the evolution of the MJO is still unclear (Lappen and Schumacher 2014; Klingaman et al. 2015; Cao and Zhang 2017) and remains a topic for future study.

We wish to objectively quantify the delay or growth time (τ) between drying in the lower and upper troposphere. To make τ relevant to the MJO, we applied bandpass (eastward 20–60 day) filtering to time series of Q_2 and M_{con} over 5°S–5°N for October 2011 through January 2012 plus buffer layers of the time mean in the beginning and end of the time series. A time–longitude diagram of filtered Q_2 in Fig. 13a shows the eastward-propagating signals of the three MJO events at 800 (colors) and 400 hPa (contours, dotted for zeros). We define τ as differences in time between zero anomalies at 800 and 400 hPa. Changes from positive to negative Q_2 at 800 hPa (blue to orange) occur several days prior to those at 400 hPa as expected from the vertically tilted structures in Fig. 12. Similar differences are shown in a time–longitude diagram of filtered M_{con} in Fig. 13b but with a shorter τ. Figure 14 shows τ of Q_2 and M_{con} over 50°–90°E and 5°S–5°N for each MJO event. The estimated τ of Q_2 is generally longer than that of M_{con} as also indicated in Figs. 12 and 13, suggesting that the actual transition time scales of convective systems could be faster (by ~1.2 days on average) than that inferred from Q_2. The result is consistent with the fast growth of convection observed in radar measurements during DYNAMO (Powell and Houze 2013). The convective evolution of the November MJO event is slower than the October event over the Indian Ocean in our estimate (Fig. 14), while the October event has a slower, longer buildup period over the DYNAMO arrays as shown in Fig. 6 as well as in Johnson et al. (2015). This is because of a much longer τ over the western than over central and eastern Indian Ocean for the November MJO as shown in Fig. 13. It is interesting that the average τ estimated from M_{con} for the December event is only 0.3 days.

c. *Radiative–convective instability*

Studies have suggested cloud radiative feedback plays an important role in the existence and maintenance of the MJO. Raymond (2001) showed that cloud–radiation interactions could make the tropical

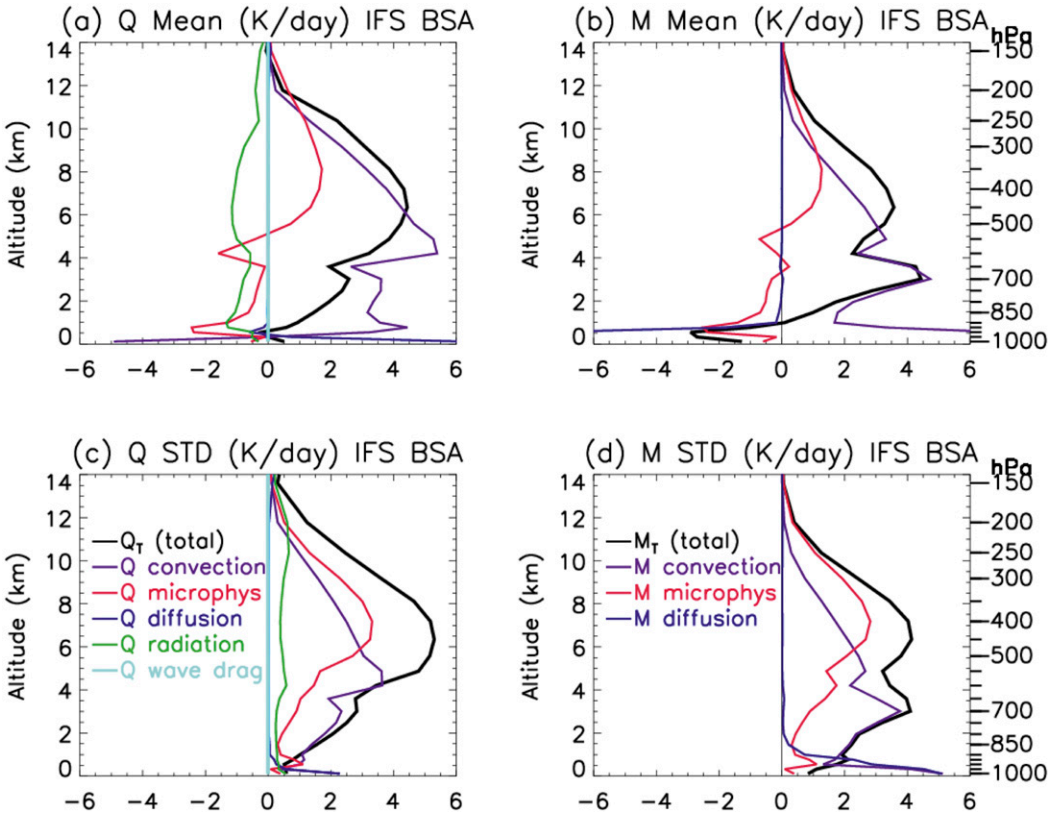

FIG. 10. Vertical profile of the (a),(b) means and (c),(d) standard deviations of (left) the total heating tendency Q_T and (right) the total drying tendency M_T by all physical processes and individual tendencies from each IFS parameterization scheme for October–December 2011 over the BSA.

atmosphere susceptible to large-scale perturbations, resulting in MJO-like oscillations. Emanuel et al. (2014) presented evidence that a radiative–convective instability can occur with high water vapor concentration in the lower troposphere. Lee et al. (2001) argued, based on Yu et al. (1998), that radiative–convective instability can exist when the ratio of anomalies in the column-integrated radiative heating to convective heating (RRC) is ~20% or greater. We note, however, that the instability that emerged in the interactive radiation simulation in Lee et al. (2001) actually produced strong westward convective propagation, while a fixed radiation case generated eastward Kelvin wavelike signals in their simulations. Several studies have attempted to determine whether the tropical atmosphere reaches radiative–convective instability for the MJO or intraseasonal oscillation based on this 20% criterion (Lin and Mapes 2004; Johnson et al. 2015; Ciesielski et al. 2017). Lin and Mapes (2004) showed that the RRC in the tropics is typically about 10%–15%. Since this ratio can be extremely high with a small amount of precipitation, a definitive value would not be a necessary condition for radiative–convective instability under all conditions. Rather, the combined effect of enhanced radiative heating and surface fluxes, moisture availability, and circulation could matter for promoting radiative–convective instability, following the idea of the normalized gross moist stability (Neelin and Held 1987; Raymond et al. 2009; Sobel and Maloney 2012). Kim et al. (2015) calculated the RRC (or greenhouse enhancement factor) based on OLR and precipitation from observations and climate model simulations and showed that it depends on the precipitation rate itself and the MJO cycle. They further demonstrated that the RRC is higher for global models that produce stronger MJO signals.

In this subsection, we show how the RRC changes with the MJO cycle over the sounding array and Indian Ocean during DYNAMO and discuss whether it is a good indicator of the conditions for radiative–convective instability. The calculation of RRC can be sensitive to how anomalies are defined. An anomaly as a deviation from a mean state could be misleading, for instance, when a radiative heating anomaly is positive and a convective heating anomaly is negative. This case must represent enhanced radiative heating, but the ratio calculation would indicate the opposite. To

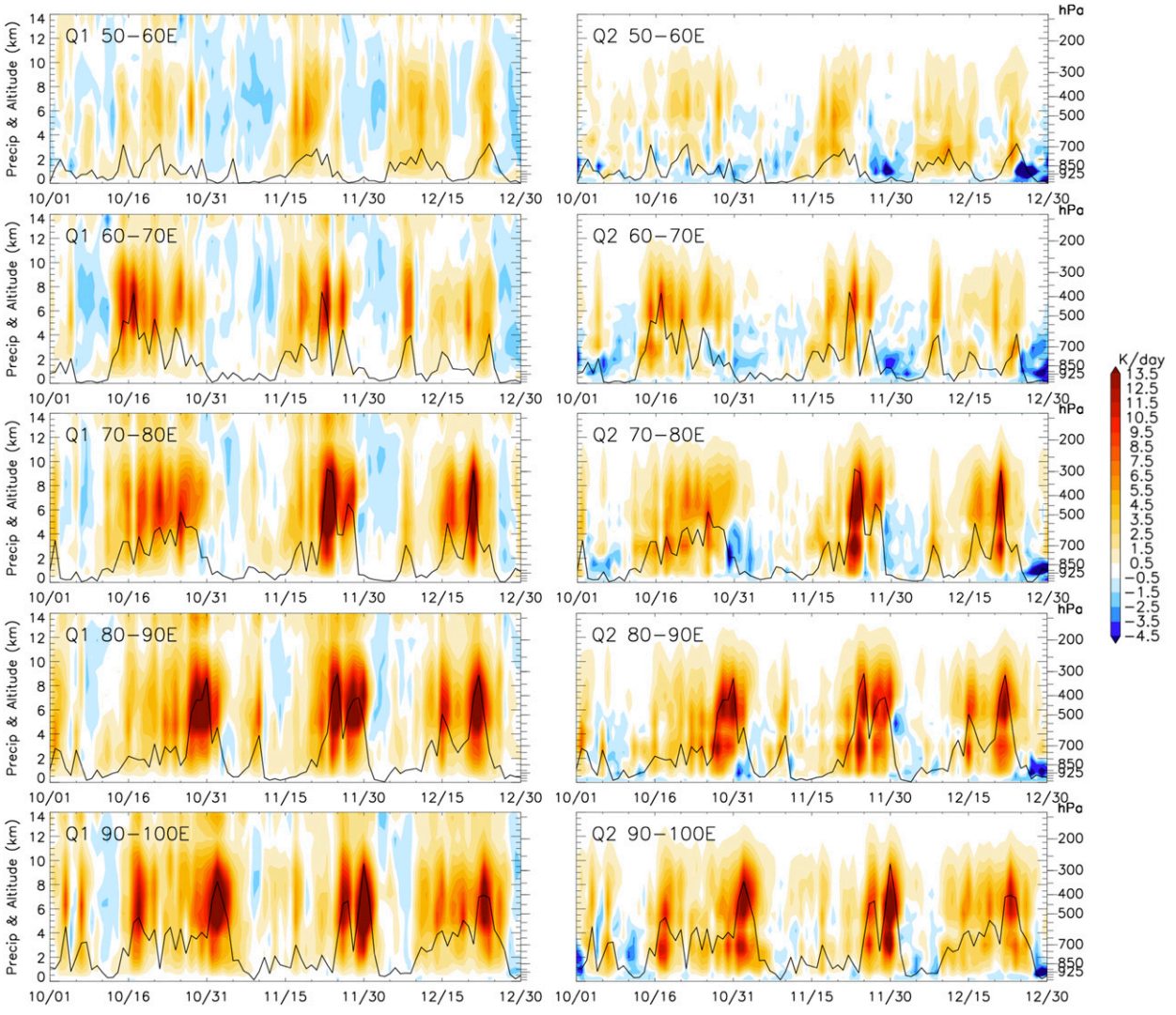

FIG. 11. Daily mean time series of IFS (left) Q_1 and (right) Q_2 averaged over 5°S–5°N for longitudes of (from top to bottom) 50°–60°, 60°–70°, 70°–80°, 80°–90°, and 90°–100°E. Black curves are TRMM precipitation (mm $6\,h^{-1}$; left ordinate).

avoid this problem of negative values of the ratio, we use a minimum value as a baseline at each grid. That is, RRC is computed as

$$\mathrm{RRC} = \frac{\langle Q_{\mathrm{rad}}\rangle - \langle Q_{\mathrm{rad}}\rangle_{\mathrm{min}}}{\langle Q_T - Q_{\mathrm{rad}}\rangle - \langle Q_T - Q_{\mathrm{rad}}\rangle_{\mathrm{min}}}, \qquad (9)$$

where angle brackets represent mass-weighted column average between 1000 to 100 hPa and convective heating ($Q_T - Q_{\mathrm{rad}} = Q_{\mathrm{con}} + Q_{\mathrm{mic}}$) is the total nonradiative diabatic heating as defined in other studies (Lee et al. 2001; Lin and Mapes 2004; Johnson et al. 2015; Ciesielski et al. 2017). The RRC over the DYNAMO arrays in IFS-RF varies significantly through the MJO cycle, ranging from ~5% up to 60% (Fig. 15, lower panel). As was also shown by Kim et al. (2015), we note that the ratio of negative OLR anomalies to precipitation (P') anomalies [e.g., $-\mathrm{OLR}'(P')/P'$] yield very similar results to RRC based on radiative and convective heating in IFS-RF (not shown). RRC is about 10%–20% during the MJO convective buildup, roughly consistent with the results from Lin and Mapes (2004). During the decay phase of the MJO, convective heating drops more quickly than radiative heating (Fig. 15, upper panel), resulting in peaks in RRC > 50%. This is consistent with results from estimates of radiative and convective heating based on DYNAMO observations and CERES data over Gan Island (Ciesielski et al. 2017). Results similar to Fig. 15 were found outside the DYNAMO arrays over the broader equatorial Indian Ocean (not shown), excluding the possibility that downstream high clouds from active convection enhance radiation to the

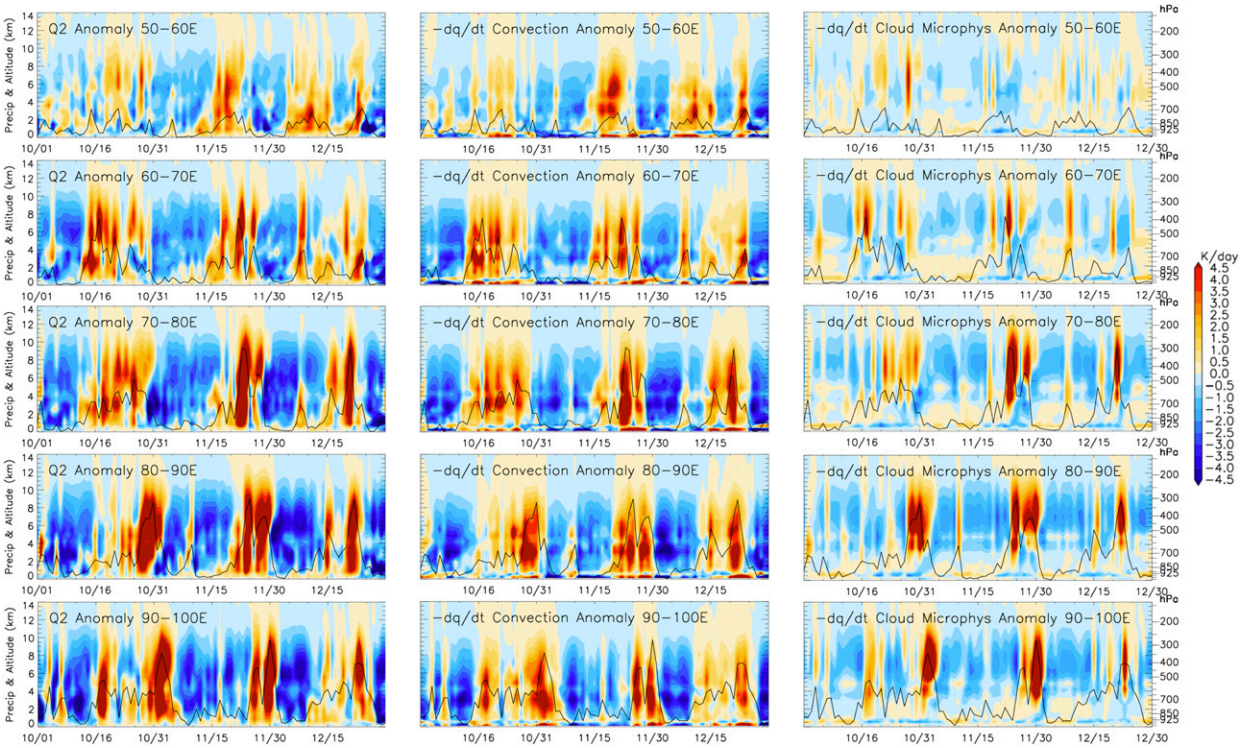

FIG. 12. As in Fig. 11, but for anomalies of IFS (left) Q_2, (middle) M_{con}, and (right) M_{mic}.

east. During the decay phase, convection is suppressed because of the advection of dry air (Sobel et al. 2014; Chikira 2014; Janiga and Zhang 2016) despite high RRC. RRC is large in the wake of the MJO as well as at other times and in other areas of weak precipitation (Fig. 16). RRC also varies with other types of convective signals other than the MJO, such as westward-propagating perturbations over the western Pacific.

Figures 17a,b compare RRCs as a function of precipitation for the increasing and decreasing MJO phases in IFS-RF. The increasing (decreasing) MJO phase is defined as a time period with a positive (negative) tendency in bandpass (eastward 20–60 day)-filtered precipitation at each grid point. The solid line for the mean RRC at each $0.2\,\text{K}\,\text{day}^{-1}$ convective heating bin indicates that the RRC is strongly dependent on precipitation. For both MJO tendencies, RRC is stronger within weaker precipitation regimes as found in Kim et al. (2015). However, RRC is much weaker during the increasing rather than the decreasing MJO phase, especially during light precipitation regimes. The larger RRC during the decay period in our results suggests that increased radiative heating might be a consequence, not a cause, of cloud development of the MJO. Kim et al. (2015) suggested that radiative feedback is important for simulating MJOs in global models because ratios are stronger during active MJO periods than nonactive periods and global models that have stronger MJO strength tend to have larger ratios. This is also true in IFS-RF but mainly because of strong ratios during a still-active but declining MJO period (the period when intraseasonal precipitation anomalies are positive but their time derivatives are negative). Our results of strong RRCs in the wake of the MJO suggest an alternative interpretation of the results from Kim et al. (2015): RRCs might be large as a consequence of strong fluctuations in clouds associated with the simulated MJO rather than its cause. We, however, emphasize that our results do not mean that radiation is only a passive variable. Results of stronger ratios during the decay phase suggest that calculations of this simple ratio could be misleading when it comes to the role of radiative feedback or the presence of radiative–convective instability. This analysis suggests a need for more observational work on radiative feedbacks as an MJO mechanism.

Instead of the RRC, a more generic measure should better represent radiative feedback on convection. Radiative feedback can be measured as changes in radiative heating versus changes in convective heating or changes in OLR versus changes in precipitation. This can be represented as a slope of radiative heating per

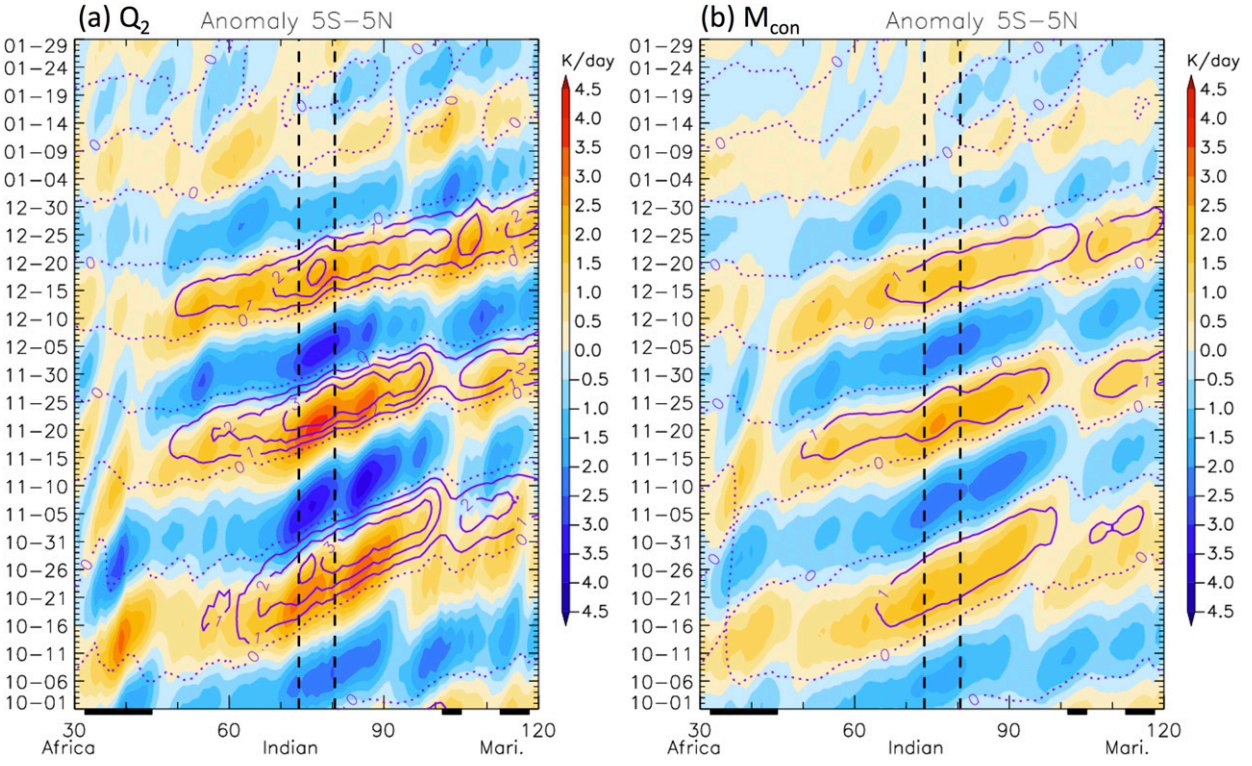

FIG. 13. Fourier-filtered anomalies of (a) Q_2 and (b) M_{con} averaged over 5°S–5°N in IFS-RF. Color shading represents signals at 800 hPa, and contours of 0 (dotted purple) and 1 to 3 (solid purple) K day^{-1} are at 400 hPa. Two dashed lines represent zonal boundaries of the DYNAMO sounding arrays.

unit convective heating (or precipitation) change as discussed in Hannah and Maloney (2014):

$$\text{Feedback} = \frac{\Delta Q_{\text{rad}}}{\Delta Q_c} = \frac{\Delta Q_{\text{rad}}}{\Delta(Q_T - Q_{\text{rad}})} \approx \frac{\Delta(-\text{OLR})}{\Delta(\text{Precipitation})}. \quad (10)$$

The three DYNAMO MJO events observed over the Indian Ocean were weakened over the Maritime Continent, and convective signals associated with the MJO disappeared over the western Pacific, in which other types of convectively coupled waves still existed (Gottschalck et al. 2013). We test whether the radiative

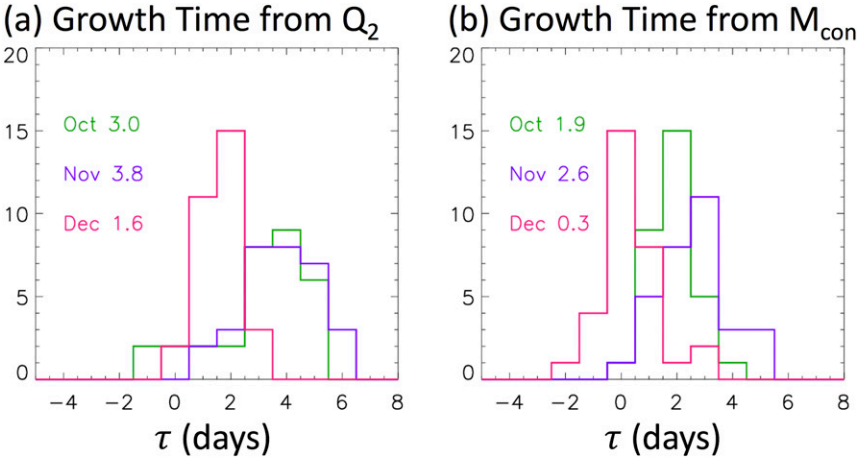

FIG. 14. Distribution of growth time τ of drying tendency from 800 to 400 hPa over 50°–90°E and 5°S–5°N for the October, November, and December MJO events calculated from (a) Q_2 and (b) M_{con} in IFS-RF.

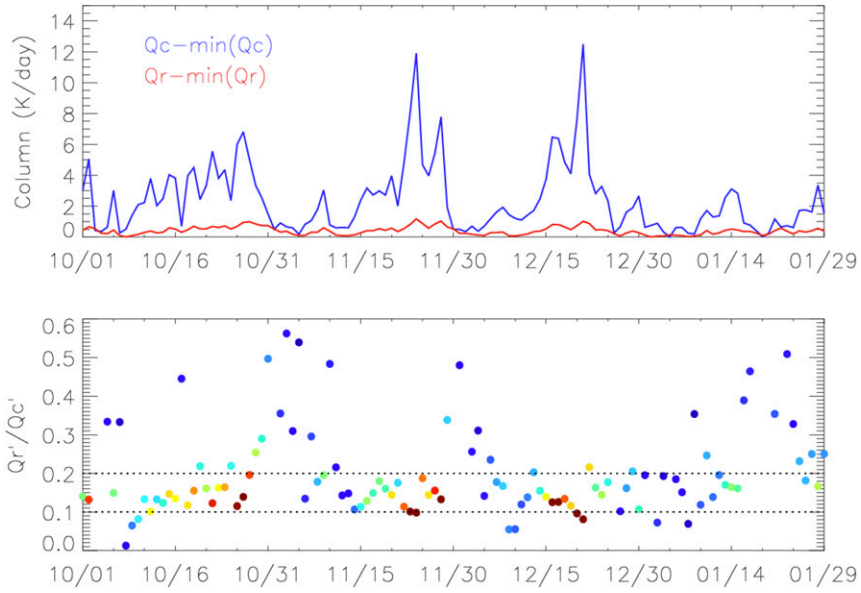

FIG. 15. (top) Daily mean time series of column-averaged heating of $Q_T - Q_{\text{rad}}$ (blue) and Q_{rad} (red) over the BSA from IFS-RF. The minimum value was subtracted for each datum. (bottom) Time series of RRC, the ratio of $\langle Q_{\text{rad}} \rangle - \langle Q_{\text{rad}} \rangle_{\text{min}}$ to $\langle Q_T - Q_{\text{rad}} \rangle_{\text{min}}$. Two dotted lines correspond to 10% and 20%. Blue to red color corresponds to weaker to stronger convective heating. $Q_T - Q_{\text{rad}} = Q_{\text{con}} + Q_{\text{mic}}$

feedback parameter calculated using Eq. (10) differs over two regions: the Indian Ocean as an MJO region and the western Pacific as a non-MJO region (Fig. 18). The feedback parameters obtained from radiative and convective heating in IFS-RF show a very similar behavior over both the MJO and non-MJO regions. They indicate that radiative feedback is generally strong in the weak convective regimes and decreases almost monotonically with increasing convective heating. The observed similarity of the feedback parameter over the two different regions suggests that radiative feedback as measured by Eq. (10) does not differentiate the MJO from other types of convection.

Upon a reviewer's suggestion, we also compared amplitudes of adiabatic cooling/heating calculated from vertical advection of heat $\overline{\omega}\partial\overline{s}/\partial p$ and diabatic heating in IFS-RF to examine whether radiative instability presented during the DYNAMO period. We found that adiabatic cooling is in general slightly greater than diabatic heating over the Indian Ocean, similar to results from MERRA-2 (Powell 2017). However, in contrast to the results from MERRA-2 that diabatic heating exceeds adiabatic cooling on the MJO scale (Powell 2017), our results from the IFS-RF show that adiabatic cooling is still slightly greater than diabatic heating for October and November MJO events, indicating that the relative amplitudes of adiabatic versus diabatic (with and without the radiative component) heating do not tell whether radiative feedback was important for the DYNAMO MJO events.

5. Summary and discussion

We have used reforecast data from the ECMWF IFS (IFS-RF) to investigate heating and moistening processes associated with the MJOs over the Indian Ocean during the DYNAMO field campaign (October 2011–January 2012). This study consists mainly of two parts. The first part validates the IFS-RF against observations over the DYNAMO sounding arrays. The second compares the IFS-RF over the DYNAMO sounding arrays to other locations along the equator over the Indian Ocean to assess the extent to which DYNAMO observations are applicable outside the DYNAMO arrays.

The IFS slightly overestimated the mean precipitation during DYNAMO compared to satellite estimates. It, however, produced reasonable variability in precipitation associated with the MJO and synoptic-scale disturbances over the sounding arrays and the propagation of the MJO over the equatorial Indian Ocean. The apparent heat source Q_1 and apparent moisture sink Q_2 from IFS-RF and DYNAMO sounding observations agree well in general with similar magnitudes and structural evolution related to the MJO except near the melting level. The vertical profiles of T, q, u, v, ω, and radiation are also well matched. These comparisons lend confidence toward using tendency

terms from IFS parameterization schemes of cumulus convection, microphysics, radiation, turbulence, and gravity wave drag to study detailed heating and moistening processes associated with the MJO over the Indian Ocean.

The Q_1 and Q_2 from the IFS-RF are dominated by the contribution from the parameterization of cumulus convection, followed by those of microphysics (heating/cooling and drying/moistening) and radiation (heating/cooling). While heating and drying by convection exhibit the typical double peak in the upper and lower troposphere, respectively, those due to microphysics and radiation reach their peaks in the upper troposphere. Turbulent diffusion provides negligible contributions to the total Q_1 and Q_2 throughout the troposphere but very strong heating and moistening near the surface. Contributions from gravity wave drag are also negligibly small in the troposphere.

The vertical growth in Q_1 and Q_2 with the progression of MJO convection is seen over the broader equatorial Indian Ocean in IFS-RF. The growth can be gradual or stepwise as observed in the DYNAMO soundings (Johnson et al. 2015). The rapid growth is more evident in the heat and moisture tendency terms produced by the cumulus scheme (Q_{con}, M_{con}), suggesting actual changes in convective systems could be faster than what appears in Q_1 and Q_2 anomalies, as was observed by radar data during DYNAMO (Powell and Houze 2013). The growth time in Q_2, defined as the time lag between 800 and 400 hPa, is longer than that in M_{con} by 1.2 days on average. When a gradual growth of Q_1 and Q_2 associated with the MJO occurs, it is attributed to evaporative cooling in the lower troposphere that is less during suppressed to buildup periods than during deep convective and stratiform periods. The eastern Indian Ocean features more widespread and continuous convective heating and drying and brief periods of convective cooling and moistening in the wake of the MJO convective peaks. These results suggest that the existence of abrupt changes in cloud populations is not uncommon. This raises a question as to whether progression of cloud populations from shallow convection to congestus through gradual moistening by clouds is always a necessary condition for promoting MJO deep convection on the intraseasonal time scale, especially over regions of persistent and strong mean precipitation such as the eastern Indian Ocean. In such a moist environment, cloud moistening effects might make it possible for the shallow-to-deep transition to take place in a shorter time than in a dry environment. The role of cloud moistening effect in the shallow-to-deep transition might vary at different stages of the MJO life cycle. It is possible that cloud moistening effects are important for the transition from shallow to deep convection during the MJO onset (Takemi; 2015; Janiga and Zhang 2016; Powell 2016) with large-scale advection of moisture playing a greater role in MJO propagation (Sobel et al. 2014; Adames and Wallace 2015; Zermeño-Díaz et al. 2015).

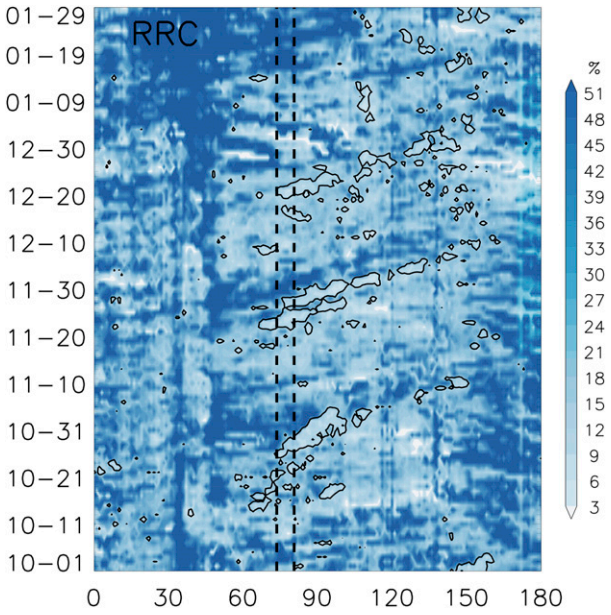

FIG. 16. Time–longitude diagram of RRC over 5°S–5°N for October 2011 to January 2012 in IFS-RF. The black contour is IFS precipitation of 20 mm day^{-1}. Two dashed lines represent zonal boundaries of the DYNAMO sounding arrays.

The IFS-produced ratio of column-integrated radiative heating anomalies to convective (nonradiative) heating anomalies (RRC) is 10%–20% over the DYNAMO arrays during the convective buildup to peak phases of the MJO. Much larger ratios occur over the equatorial Indian Ocean during the decay phase of the MJO and other areas of minimum precipitation. The RRC fluctuates in time and space primarily in response to the variability of precipitation (latent heating). By itself, it can hardly be considered a measure of the contribution of radiation to the development of convective instability. In a dispersive moist wave theory of the MJO (Adames and Kim 2016), the zonal-scale selection of the MJO depends on a greenhouse enhancement or cloud–radiation feedback parameter, which is equivalent to the RRC. This parameter or ratio increases monotonically with decreasing zonal wavenumber (Fig. 8d of Adames and Kim 2016). Although our results show variations in the ratio with the MJO cycle, greater RRCs associated with the MJO arise from enhanced radiative heating during the decay period after a peak in precipitation. The increased ratio during a decay convective phase cannot necessarily be considered as a result of increased radiative feedback, and the zonal wavenumber dependence of the ratio is expected to be observed regardless the existence of radiative feedback because of its dependence on the MJO

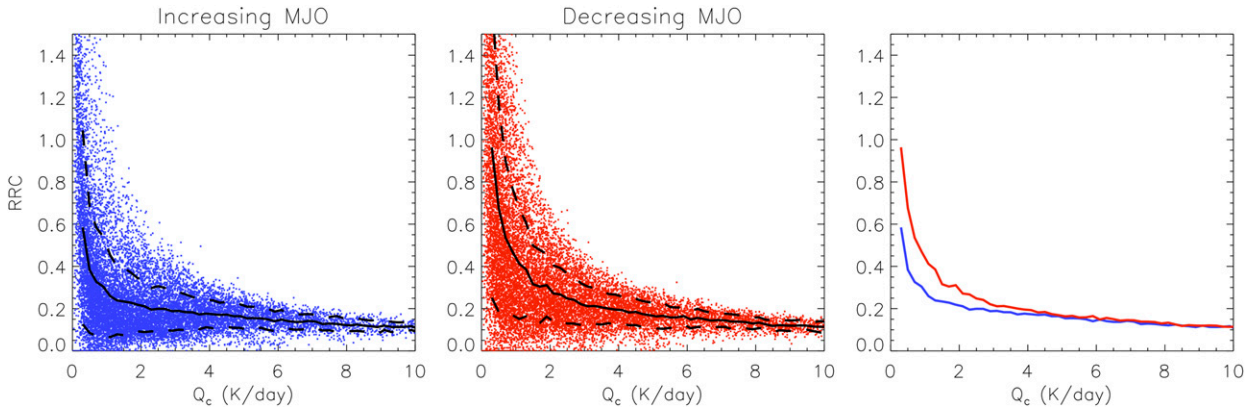

FIG. 17. RRC as a function of convective heating in IFS for the phases of (left) increasing MJO and (middle) decreasing MJO over 60°–90°E and 5°S–5°N for October–December 2011. Individual dots represent ratios at each grid point. Solid line is the mean and dashed line is ±1 standard deviation from the mean at each 0.2 K day^{-1} convective heating bin. (right) The mean ratio for the increasing (blue) and decreasing (red) MJO phases are given. The ratios during the decreasing MJO phase are statistically larger than those during the increasing phase at convective heating ranges up to 4.8 K day^{-1} at the 95% confidence level based on the Student's *t* test.

cycle. The correlation between the RRC and MJO strength in global model simulations (Kim et al. 2015) might be a consequence, not a cause, of different model capabilities of reproducing the MJO. This by no means invalidates the dispersive moist wave theory of the MJO. However, causal relationships between the zonal-scale selection of the MJO and wavenumber dependence of the RRC and similar ratios need to be further investigated.

Two alternative approaches, namely, changes in radiative heating per unit of changes in convective heating (Hannah and Maloney 2014) and amplitudes of adiabatic versus diabatic heating rates (Powell 2017), are applied to IFS-RF to measure the possible role of radiative feedback in the MJO. Neither of them unambiguously distinguishes radiative feedback in the MJO and non-MJO convective events. Further detailed studies on interactions between radiation, convection, and circulations associated with the MJO as well as non-MJO convective events, such as convectively coupled equatorial waves, are needed to gain better insights into the possible role of radiation in the MJO. Based on the results of this study, it appears that reforecast data such as the IFS-RF can be very useful for this purpose.

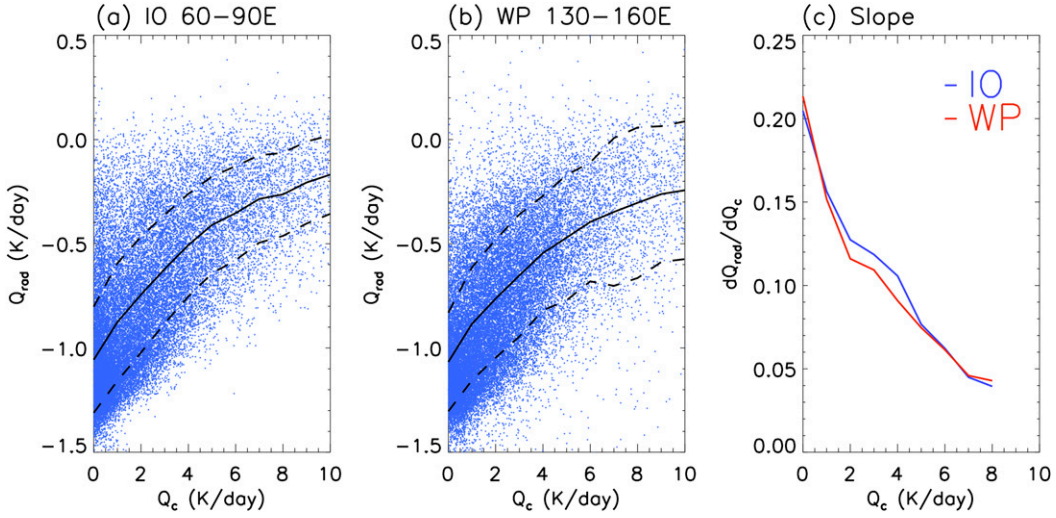

FIG. 18. Radiative heating as a function of convective heating in IFS-RF over the equatorial (5°S–5°N) (a) Indian Ocean (60°–90°E) and (b) western Pacific (130°–160°E) for October–December 2011. Individual dots represent data at each grid point. Solid black line is the mean at each 1 K day^{-1} convective heating bin, and dashed lines represent 1 standard deviation from the mean. (c) Comparison of a radiative feedback parameter, $\Delta Q_{\mathrm{rad}}/\Delta Q_c$, calculated as a slope of radiative heating per unit convective heating over the Indian Ocean (blue) and western Pacific (red).

Acknowledgments. The authors thank Walter Hannah, Scott Powell, and an anonymous reviewer for their insightful and constructive comments on an early version of the article. JEK thanks the Joint Institute for the Study of the Atmosphere and Ocean (JISAO) for hosting her visit during which this manuscript was drafted. This study was supported by NSF Grant AGS-1450582 (JEK and CZ) and NOAA Grant NA13OAR4310161 (CZ). This paper is PMEL Contribution 4669. The IFS reforecast data are available from NCAR EOL. Other data are available online [http://johnson.atmos.colostate.edu/dynamo (DYNAMO soundings), https://mirador.gsfc.nasa.gov (TRMM 3B42), ftp://ftp.cgd.ucar.edu/archive/PRECIP (GPCP), https://www.arm.gov/research/campaigns/amf2011amie-gan (CombRet), and https://ceres.larc.nasa.gov (CERES)].

REFERENCES

Adames, Á. F., and J. M. Wallace, 2015: Three-dimensional structure and evolution of the moisture field in the MJO. *J. Atmos. Sci.*, **72**, 3733–3754, https://doi.org/10.1175/JAS-D-15-0003.1.

——, and D. Kim, 2016: The MJO as a dispersive, convectively coupled moisture wave: Theory and observations. *J. Atmos. Sci.*, **73**, 913–941, https://doi.org/10.1175/JAS-D-15-0170.1.

Bechtold, P., M. Köhler, T. Jung, F. Doblas-Reyes, M. Leutbecher, M. J. Rodwell, F. Vitart, and G. Balsamo, 2008: Advances in predicting atmospheric variability with the ECMWF model: From synoptic to decadal time-scales. *Quart. J. Roy. Meteor. Soc.*, **134**, 1337–1351, https://doi.org/10.1002/qj.289.

——, N. Semane, P. Lopez, J.-P. Chaboureau, A. Beljaars, and N. Bormann, 2014: Representing equilibrium and non-equilibrium convection in large-scale models. *J. Atmos. Sci.*, **71**, 734–753, https://doi.org/10.1175/JAS-D-13-0163.1.

Benedict, J. J., and D. Randall, 2007: Observed characteristics of the MJO relative to maximum rainfall. *J. Atmos. Sci.*, **64**, 2332–2354, https://doi.org/10.1175/JAS3968.1.

Bretherton, C. S., M. E. Peters, and L. E. Back, 2004: Relationships between water vapor path and precipitation over the tropical oceans. *J. Climate*, **17**, 1517–1528, https://doi.org/10.1175/1520-0442(2004)017<1517:RBWVPA>2.0.CO;2.

Cao, G., and G. J. Zhang, 2017: Role of vertical structure of convective heating in MJO simulation in NCAR CAM5.3. *J. Climate*, **30**, 7423–7439, https://doi.org/10.1175/JCLI-D-16-0913.1.

Chen, S., and Coauthors, 2015: A study of CINDY/DYNAMO MJO suppressed phase. *J. Atmos. Sci.*, **72**, 3755–3779, https://doi.org/10.1175/JAS-D-13-0348.1.

Chikira, M., 2014: Eastward-propagating intraseasonal oscillation represented by Chikira–Sugiyama cumulus parameterization. Part II: Understanding moisture variation under weak temperature gradient balance. *J. Atmos. Sci.*, **71**, 615–639, https://doi.org/10.1175/JAS-D-13-038.1.

Ciesielski, P. E., and Coauthors, 2014: Quality-controlled upper-air sounding dataset for DYNAMO/CINDY/AMIE: Development and corrections. *J. Atmos. Oceanic Technol.*, **31**, 741–764, https://doi.org/10.1175/JTECH-D-13-00165.1.

——, R. H. Johnson, X. Jiang, Y. Zhang, and S. Xie, 2017: Relationships between radiation, clouds, and convection during DYNAMO. *J. Geophys. Res. Atmos.*, **122**, 2529–2548, https://doi.org/10.1002/2016JD025965.

Del Genio, A. D., and Y. Chen, 2015: Cloud-radiative driving of the Madden-Julian oscillation as seen by the A-Train. *J. Geophys. Res. Atmos.*, **120**, 5344–5356, https://doi.org/10.1002/2015JD023278.

Emanuel, K., A. A. Wing, and E. M. Vincent, 2014: Radiative-convective instability. *J. Adv. Model. Earth Syst.*, **6**, 75–90, https://doi.org/10.1002/2013MS000270.

Esbensen, S., J.-T. Wang, and E. I. Tollerud, 1988: A composite life cycle of nonsquall mesoscale convective systems over the tropical ocean. Part II: Heat and moisture budgets. *J. Atmos. Sci.*, **45**, 537–548, https://doi.org/10.1175/1520-0469(1988)045<0537:ACLCON>2.0.CO;2.

Feng, Z., S. A. McFarlane, C. Schumacher, S. Ellis, and N. Bharadwaj, 2014: Constructing a merged cloud–precipitation radar dataset for tropical clouds during the DYNAMO/AMIE experiment on Addu Atoll. *J. Atmos. Oceanic Technol.*, **31**, 1021–1042, https://doi.org/10.1175/JTECH-D-13-00132.1.

Forbes, R., and A. M. Tompkins, 2011: An improved representation of cloud and precipitation. *ECMWF Newsletter*, No. 129, ECMWF, Reading, United Kingdom, 13–18.

——, ——, and A. Untch, 2011: A new prognostic bulk microphysics scheme for the IFS. ECMWF Tech. Memo. 649, 30 pp.

Fu, X., W. Wang, J.-Y. Lee, B. Wang, K. Kikuchi, J. Xu, J. Li, and S. Weaver, 2015: Distinctive roles of air–sea coupling on different MJO events: A new perspective revealed from the DYNAMO/CINDY field campaign. *Mon. Wea. Rev.*, **143**, 794–812, https://doi.org/10.1175/MWR-D-14-00221.1.

Gottschalck, J., P. E. Roundy, C. J. Schreck III, A. Vintzileos, and C. Zhang, 2013: Large-scale atmospheric and oceanic conditions during the 2011–12 DYNAMO field campaign. *Mon. Wea. Rev.*, **141**, 4173–4196, https://doi.org/10.1175/MWR-D-13-00022.1.

Hagos, S., Z. Feng, C. D. Burleyson, K.-S. S. Lim, C. N. Long, D. Wu, and G. Thompson, 2014a: Evaluation of convection-permitting model simulations of cloud populations associated with the Madden-Julian oscillation using data collected during the AMIE/DYNAMO field campaign. *J. Geophys. Res. Atmos.*, **119**, 12 052–12 068, https://doi.org/10.1002/2014JD022143.

——, ——, K. Landu, and C. N. Long, 2014b: Advection, moistening, and shallow-to-deep convection transitions during the initiation and propagation of Madden-Julian oscillation. *J. Adv. Model. Earth Syst.*, **6**, 938–949, https://doi.org/10.1002/2014MS000335.

Hannah, W. M., and E. D. Maloney, 2014: The moist static energy budget in NCAR CAM5 hindcasts during DYNAMO. *J. Adv. Model. Earth Syst.*, **6**, 420–440, https://doi.org/10.1002/2013MS000272.

——, B. E. Mapes, and G. S. Elsaesser, 2016: A Lagrangian view of moisture dynamics during DYNAMO. *J. Atmos. Sci.*, **73**, 1967–1985, https://doi.org/10.1175/JAS-D-15-0243.1.

Huffman, G. J., R. F. Adler, M. M. Morrissey, D. T. Bolvin, S. Curtis, R. Joyce, B. McGavock, and J. Susskind, 2001: Global precipitation at one-degree daily resolution from multisatellite observations. *J. Hydrometeor.*, **2**, 36–50, https://doi.org/10.1175/1525-7541(2001)002<0036:GPAODD>2.0.CO;2.

——, ——, D. T. Bolvin, G. Gu, E. J. Nelkin, K. P. Bowman, E. F. Stocker, and D. B. Wolff, 2007: The TRMM Multisatellite Precipitation Analysis: Quasi-global, multiyear, combined-sensor precipitation estimates at fine scale. *J. Hydrometeor.*, **8**, 38–55, https://doi.org/10.1175/JHM560.1.

Janiga, M. A., and C. Zhang, 2016: MJO moisture budget during DYNAMO in a cloud-resolving model. *J. Atmos. Sci.*, **73**, 2257–2278, https://doi.org/10.1175/JAS-D-14-0379.1.

Johnson, R. H., 1984: Partitioning tropical heat and moisture budgets into cumulus and mesoscale components: Implications

for cumulus parameterization. *Mon. Wea. Rev.*, **112**, 1590–1601, https://doi.org/10.1175/1520-0493(1984)112<1590:PTHAMB>2.0.CO;2.

——, and P. E. Ciesielski, 2013: Structure and properties of Madden–Julian oscillations deduced from DYNAMO sounding arrays. *J. Atmos. Sci.*, **70**, 3157–3179, https://doi.org/10.1175/JAS-D-13-065.1.

——, T. M. Rickenbach, S. A. Rutledge, P. E. Ciesielski, and W. H. Schubert, 1999: Trimodal characteristics of tropical convection. *J. Climate*, **12**, 2397–2418, https://doi.org/10.1175/1520-0442(1999)012<2397:TCOTC>2.0.CO;2.

——, P. E. Ciesielski, J. H. Ruppert, and M. Katsumata, 2015: Sounding-based thermodynamic budgets for DYNAMO. *J. Atmos. Sci.*, **72**, 598–622, https://doi.org/10.1175/JAS-D-14-0202.1.

Katsumata, M., P. E. Ciesielski, and R. H. Johnson, 2011: Evaluation of budget analysis during MISMO. *J. Appl. Meteor. Climatol.*, **50**, 241–254, https://doi.org/10.1175/2010JAMC2515.1.

Kerns, B. W., and S. S. Chen, 2014: Equatorial dry air intrusion and related synoptic variability in MJO initiation during DYNAMO. *Mon. Wea. Rev.*, **142**, 1326–1343, https://doi.org/10.1175/MWR-D-13-00159.1.

Kikuchi, K., G. N. Kiladis, J. Dias, and T. Nasuno, 2018: Convectively coupled equatorial waves within the MJO during CINDY/DYNAMO: Slow Kelvin waves as building blocks. *Climate Dyn.*, https://doi.org/10.1007/s00382-017-3869-5, in press.

Kim, D., M. Ahn, I. Kang, and A. D. Del Genio, 2015: Role of longwave cloud–radiation feedback in the simulation of the Madden–Julian oscillation. *J. Climate*, **28**, 6979–6994, https://doi.org/10.1175/JCLI-D-14-00767.1.

Kim, J.-E., and Coauthors, 2016: Ubiquitous influence of waves on tropical high cirrus clouds. *Geophys. Res. Lett.*, **43**, 5895–5901, https://doi.org/10.1002/2016GL069293.

Klingaman, N. P., and Coauthors, 2015: Vertical structure and diabatic processes of the Madden–Julian oscillation: Linking hindcast fidelity to simulated diabatic heating and moistening. *J. Geophys. Res. Atmos.*, **120**, 4690–4717, https://doi.org/10.1002/2014JD022374.

Kubota, H., K. Yoneyama, J. I. Hamada, P. Wu, A. Sudaryanto, and I. B. Wahyono, 2015: Role of Maritime Continent convection during the preconditioning stage of the Madden-Julian oscillation observed in CINDY2011/DYNAMO. *J. Meteor. Soc. Japan*, **93**, 101–114, https://doi.org/10.2151/jmsj.2015-050.

Lappen, C.-L., and C. Schumacher, 2014: The role of tilted heating in the evolution of the MJO. *J. Geophys. Res. Atmos.*, **119**, 2966–2989, https://doi.org/10.1002/2013JD020638.

Lee, M.-I., I.-S. Kang, J.-K. Kim, and B. E. Mapes, 2001: Influence of cloud-radiation interaction on simulating tropical intraseasonal oscillation with an atmosphere general circulation model. *J. Geophys. Res.*, **106**, 14 291–14 233, https://doi.org/10.1029/2001JD900143.

Li, T., C. Zhao, P. C. Hsu, and T. Nasuno, 2015: MJO initiation processes over the tropical Indian Ocean during DYNAMO/CINDY2011. *J. Climate*, **28**, 2121–2135, https://doi.org/10.1175/JCLI-D-14-00328.1.

Li, X., W. Tao, A. P. Khain, J. Simpson, and D. E. Johnson, 2009: Sensitivity of a cloud-resolving model to bulk and explicit bin microphysical schemes. Part I: Comparisons. *J. Atmos. Sci.*, **66**, 3–21, https://doi.org/10.1175/2008JAS2646.1.

Lin, J.-L., and B. E. Mapes, 2004: Radiation budget of the tropical intraseasonal oscillation. *J. Atmos. Sci.*, **61**, 2050–2062, https://doi.org/10.1175/1520-0469(2004)061<2050:RBOTTI>2.0.CO;2.

Ling, J., and C. Zhang, 2011: Structural evolution in heating profiles of the MJO in global reanalyses and TRMM retrievals. *J. Climate*, **24**, 825–842, https://doi.org/10.1175/2010JCLI3826.1.

——, P. Bauer, P. Bechtold, A. Beljaars, R. Forbes, F. Vitart, M. Ulate, and C. Zhang, 2014: Global versus local MJO forecast skill of the ECMWF model during DYNAMO. *Mon. Wea. Rev.*, **142**, 2228–2247, https://doi.org/10.1175/MWR-D-13-00292.1.

Madden, R. A., and P. R. Julian, 1971: Detection of a 40–50-day oscillation in the zonal wind in the tropical Pacific. *J. Atmos. Sci.*, **28**, 702–708, https://doi.org/10.1175/1520-0469(1971)028<0702:DOADOI>2.0.CO;2.

——, and ——, 1972: Description of global-scale circulation cells in the tropics with a 40–50-day period. *J. Atmos. Sci.*, **29**, 1109–1123, https://doi.org/10.1175/1520-0469(1972)029<1109:DOGSCC>2.0.CO;2.

Mapes, B. E., and J. T. Bacmeister, 2012: Diagnosis of tropical biases and the MJO from patterns in the MERRA analysis tendency fields. *J. Climate*, **25**, 6202–6214, https://doi.org/10.1175/JCLI-D-11-00424.1.

Miyakawa, T., andCoauthors, 2014: Madden–Julian oscillation prediction skill of a new-generation global model demonstrated using a supercomputer. *Nat. Commun.*, **5**, 3769, https://doi.org/10.1038/ncomms4769.

Moncrieff, M. W., D. E. Waliser, M. J. Miller, M. E. Shapiro, G. Asrar, and J. Caughey, 2012: Multiscale convective organization and the YOTC virtual global field campaign. *Bull. Amer. Meteor. Soc.*, **93**, 1171–1187, https://doi.org/10.1175/BAMS-D-11-00233.1.

Nagarajan, B., and A. R. Aiyyer, 2004: Performance of the ECMWF operational analyses over the tropical Indian Ocean. *Mon. Wea. Rev.*, **132**, 2275–2282, https://doi.org/10.1175/1520-0493(2004)132<2275:POTEOA>2.0.CO;2.

Nasuno, T., T. Li, and K. Kikuchi, 2015: Moistening processes before the convective initiation of Madden–Julian oscillation events during the CINDY2011/DYNAMO period. *Mon. Wea. Rev.*, **143**, 622–643, https://doi.org/10.1175/MWR-D-14-00132.1.

Neelin, J. D., and I. M. Held, 1987: Modeling tropical convergence based on the moist static energy budget. *Mon. Wea. Rev.*, **115**, 3–12, https://doi.org/10.1175/1520-0493(1987)115<0003:MTCBOT>2.0.CO;2.

Oh, J. H., X. Jiang, D. E. Waliser, M. W. Moncrieff, R. H. Johnson, and P. Ciesielski, 2015: A momentum budget analysis of westerly wind events associated with the Madden–Julian oscillation during DYNAMO. *J. Atmos. Sci.*, **72**, 3780–3799, https://doi.org/10.1175/JAS-D-15-0044.1.

Pilon, R., C. Zhang, and J. Dudhia, 2016: Roles of deep and shallow convection and microphysics in the MJO simulated by the Model for Prediction Across Scales. *J. Geophys. Res. Atmos.*, **121**, 10 575–10 600, https://doi.org/10.1002/2015JD024697.

Powell, S. W., 2016: Updraft buoyancy within and moistening by cumulonimbi prior to MJO convective onset in a regional model. *J. Atmos. Sci.*, **73**, 2913–2934, https://doi.org/10.1175/JAS-D-15-0326.1.

——, 2017: Successive MJO propagation in MERRA-2 reanalysis. *Geophys. Res. Lett.*, **44**, 5178–5186, https://doi.org/10.1002/2017GL073399.

——, and R. A. Houze Jr., 2013: The cloud population and onset of the Madden-Julian oscillation over the Indian Ocean during DYNAMO-AMIE. *J. Geophys. Res. Atmos.*, **118**, 11 979–11 995, https://doi.org/10.1002/2013JD020421.

Raymond, D. J., 2001: A new model of the Madden–Julian oscillation. *J. Atmos. Sci.*, **58**, 2807–2819, https://doi.org/10.1175/1520-0469(2001)058<2807:ANMOTM>2.0.CO;2.

——, S. L. Sessions, A. H. Sobel, and Z. Fuchs, 2009: The mechanics of gross moist stability. *J. Adv. Model. Earth Syst.*, **1** (3), https://doi.org/10.3894/JAMES.2009.1.9.

Rienecker, M. M., and Coauthors, 2011: MERRA: NASA's Modern-Era Retrospective Analysis for Research and Applications. *J. Climate*, **24**, 3624–3648, https://doi.org/10.1175/JCLI-D-11-00015.1.

Skyllingstad, E. D., and S. P. de Szoeke, 2015: Cloud-resolving large-eddy simulation of tropical convective development and surface fluxes. *Mon. Wea. Rev.*, **143**, 2441–2458, https://doi.org/10.1175/MWR-D-14-00247.1.

Sobel, A., and E. D. Maloney, 2012: An idealized semi-empirical framework for modeling the Madden–Julian oscillation. *J. Atmos. Sci.*, **69**, 1691–1705, https://doi.org/10.1175/JAS-D-11-0118.1.

——, S. Wang, and D. Kim, 2014: Moist static energy budget of the MJO during DYNAMO. *J. Atmos. Sci.*, **71**, 4276–4291, https://doi.org/10.1175/JAS-D-14-0052.1.

Takemi, T., 2015: Relationship between cumulus activity and environmental moisture during the CINDY2011/DYNAMO field experiment as revealed from convection-resolving simulations. *J. Meteor. Soc. Japan*, **93**, 41–58, https://doi.org/10.2151/jmsj.2015-035.

Tao, W.-K., D. Johnson, C.-L. Shie, and J. Simpson, 2004: The atmospheric energy budget and large-scale precipitation efficiency of convective systems during TOGA COARE, GATE, SCSMEX, and ARM: Cloud-resolving model simulations. *J. Atmos. Sci.*, **61**, 2405–2423, https://doi.org/10.1175/1520-0469(2004)061<2405:TAEBAL>2.0.CO;2.

Tiedtke, M., 1989: A comprehensive mass flux scheme for cumulus parameterization in large-scale models. *Mon. Wea. Rev.*, **117**, 1779–1800, https://doi.org/10.1175/1520-0493(1989)117<1779:ACMFSF>2.0.CO;2.

——, 1993: Representation of clouds in large-scale models. *Mon. Wea. Rev.*, **121**, 3040–3061, https://doi.org/10.1175/1520-0493(1993)121<3040:ROCILS>2.0.CO;2.

Tompkins, A. M., K. Gierens, and G. Rädel, 2007: Ice supersaturation in the ECMWF integrated forecast system. *Quart. J. Roy. Meteor. Soc.*, **133**, 53–63, https://doi.org/10.1002/qj.14.

Tseng, K. C., C. H. Sui, and T. Li, 2015: Moistening processes for Madden–Julian oscillations during DYNAMO/CINDY. *J. Climate*, **28**, 3041–3057, https://doi.org/10.1175/JCLI-D-14-00416.1.

Virts, K. S., and J. M. Wallace, 2014: Observations of temperature, wind, cirrus, and trace gases in the tropical tropopause transition layer during the MJO. *J. Atmos. Sci.*, **71**, 1143–1157, https://doi.org/10.1175/JAS-D-13-0178.1.

Waliser, D. E., and Coauthors, 2012: The "Year" of Tropical Convection (May 2008–April 2010): Climate variability and weather highlights. *Bull. Amer. Meteor. Soc.*, **93**, 1189–1218, https://doi.org/10.1175/2011BAMS3095.1.

Wang, S., A. H. Sobel, A. Fridland, Z. Feng, J. M. Comstock, P. Minnis, and M. L. Nordeen, 2015: Simulations of cloud-radiation interaction using large-scale forcing derived from the CINDY/DYNAMO northern sounding array. *J. Adv. Model. Earth Syst.*, **7**, 1472–1498, https://doi.org/10.1002/2015MS000461.

——, ——, and J. Nie, 2016: Modeling the MJO in a cloud-resolving model with parameterized large-scale dynamics: Vertical structure, radiation, and horizontal advection of dry air. *J. Adv. Model. Earth Syst.*, **8**, 121–139, https://doi.org/10.1002/2015MS000529.

Wielicki, B. A., B. R. Barkstrom, E. F. Harrison, R. B. Lee III, G. L. Smith, and J. E. Cooper, 1996: Clouds and the Earth's Radiant Energy System (CERES): An Earth Observing System experiment. *Bull. Amer. Meteor. Soc.*, **77**, 853–868, https://doi.org/10.1175/1520-0477(1996)077<0853:CATERE>2.0.CO;2.

Xu, W., and S. A. Rutledge, 2015: Morphology, intensity, and rainfall production of MJO convection: Observations from DYNAMO shipborne radar and TRMM. *J. Atmos. Sci.*, **72**, 623–640, https://doi.org/10.1175/JAS-D-14-0130.1.

——, and ——, 2016: Time scales of shallow-to-deep convective transition associated with the onset of Madden-Julian oscillations. *Geophys. Res. Lett.*, **43**, 2880–2888, https://doi.org/10.1002/2016GL068269.

Yanai, M., S. Esbensen, and J.-H. Chu, 1973: Determination of bulk properties of tropical cloud clusters from large-scale heat and moisture budgets. *J. Atmos. Sci.*, **30**, 611–627, https://doi.org/10.1175/1520-0469(1973)030<0611:DOBPOT>2.0.CO;2.

Yang, Q., Q. Fu, and Y. Hu, 2010: Radiative impacts of clouds in the tropical tropopause layer. *J. Geophys. Res.*, **115**, D00H12, https://doi.org/10.1029/2009JD012393.

Yokoi, S., and A. H. Sobel, 2015: Seasonal march and intraseasonal variability of the moist static energy budget over the eastern Maritime Continent during CINDY2001/DYNAMO. *J. Meteor. Soc. Japan*, **93**, 81–100, https://doi.org/10.2151/jmsj.2015-041.

Yoneyama, K., C. Zhang, and C. N. Long, 2013: Tracking pulses of the Madden–Julian oscillation. *Bull. Amer. Meteor. Soc.*, **94**, 1871–1891, https://doi.org/10.1175/BAMS-D-12-00157.1.

Yu, J.-Y., C. Chou, and J. D. Neelin, 1998: Estimating the gross moist stability of the tropical atmosphere. *J. Atmos. Sci.*, **55**, 1354–1372, https://doi.org/10.1175/1520-0469(1998)055<1354:ETGMSO>2.0.CO;2.

Zermeño-Díaz, D. M., C. Zhang, P. Kollias, and H. Kalesse, 2015: The role of shallow cloud moistening in MJO and non-MJO convective events over the ARM Manus site. *J. Atmos. Sci.*, **72**, 4797–4820, https://doi.org/10.1175/JAS-D-14-0322.1.

Zhang, C., and J. Ling, 2012: Potential vorticity of the Madden–Julian oscillation. *J. Atmos. Sci.*, **69**, 65–78, https://doi.org/10.1175/JAS-D-11-081.1.